

Interface band engineering in LaAlO₃/SrTiO₃ heterostructures

J. Gabel^{1,2}, M. Schmitt¹, P. Scheiderer¹, M. Zapf¹, M. Stübinger¹, S. Huang¹, C. Schlueter^{2,3}, T.-L. Lee², M. Sing¹ and R. Claessen¹

¹Physikalisches Institut and Würzburg-Dresden Cluster of Excellence *ct.qmat*, Universität Würzburg, D-97074 Würzburg, Germany

²Diamond Light Source Ltd., Didcot, Oxfordshire OX11 0DE, United Kingdom

³Photon Science, Deutsches Elektronen-Synchrotron DESY, D-22607 Hamburg, Germany

 (Received 8 July 2022; revised 9 May 2023; accepted 14 June 2023; published 17 July 2023)

Novel two-dimensional electron systems at the interfaces of oxide heterostructures, such as LaAlO₃/SrTiO₃, have attracted much attention as they open a new route to harness the rich quantum phases of transition-metal oxides (TMOs) for potentially useful functionalities not available in conventional semiconductor electronics. For such applications, the controllability of these interface properties is key. For LaAlO₃/SrTiO₃, previous theoretical and experimental investigations of the band offset and the potential profile near the interface have yielded not only quantitatively different but sometimes even contradictory results, e.g., the absence vs presence of a potential gradient in the LaAlO₃ film. By analyzing angle-dependent hard x-ray photoelectron spectroscopy (HAXPES) data with a Poisson-Schrödinger model, we determine the charge carrier distribution and the valence band edge profile across the LaAlO₃/SrTiO₃ interface self-consistently. By systematically controlling the oxygen vacancy concentration, i.e., the doping level, during the photoemission experiments, we derive a comprehensive picture of the band scheme and show that the two-dimensional electron system is always narrowly confined to the interface. We observe a crossover of the band alignment from type II to type I with increasing doping level, which reconciles the striking inconsistencies among the earlier studies. We further find that the strongly nonlinear dielectric response of the SrTiO₃ substrates to the electric field is essential for the understanding of the band arrangement at the LaAlO₃/SrTiO₃ heterointerface.

DOI: [10.1103/PhysRevB.108.045125](https://doi.org/10.1103/PhysRevB.108.045125)

I. INTRODUCTION

The rich phase diagram of transition-metal oxides (TMOs) exhibits many quantum states with potentially useful functionalities for future novel electronic devices that cannot be realized in conventional semiconductors [1]. Recent advances in the epitaxy of TMO thin films have also enabled the exploitation of emergent *interfacial* phenomena in oxide heterostructures [2–4]. A case in point is the prototypical LaAlO₃/SrTiO₃ heterointerface. When a LaAlO₃ film is epitaxially deposited on SrTiO₃, a two-dimensional electron system (2DES) forms at the interface between the two band insulators [2]. It displays several other remarkable properties such as Rashba spin-orbit coupling [5], superconductivity [6], and coexisting ferromagnetism [3]. Electric-field gating [7] has also been demonstrated, which is essential for electronic applications like, e.g., all-oxide transistors [8]. Memristive behavior [9,10] and highly efficient and tunable spin-to-charge conversion [11,12] have also been reported.

For fundamental research as well as for potential applications it is of paramount importance to understand and control the emergent phenomena at such interfaces, i.e., engineer the band diagram [13–15]. For semiconductor heterostructures nowadays density functional theory (DFT) is routinely used to understand and describe the electronic structure and band scheme, which is, however, often inadequate for TMOs. Such calculations rely on weak electron-electron interactions, which is an incorrect starting point for materials with localized valence orbitals such as the open 3*d* shell in TMOs [16].

Modelling the band scheme in theory is further complicated by ill-defined oxygen stoichiometries [17] and high dielectric permittivities [18,19], which introduce long-range forces competing with the short-range interactions. In light of the difficulties in providing an accurate theoretical description of the band scheme, experimental insight is crucial. The only method providing *direct* access to the complete band scheme of the occupied part of the electronic structure and the microscopic electronic properties is photoemission spectroscopy [20].

Yet, the wealth of photoemission literature on the prototypical LaAlO₃/SrTiO₃ heterostructure [21] displays a surprising amount of inconsistencies and striking contradictions, as summarized in Table I. For example, some studies classify the LaAlO₃/SrTiO₃ heterointerface as a type II interface while others find a type I interface. Estimates for the depth of the confining potential and the extension of the 2DES are scarce and differ widely [25,26,29,30]. It is, in particular, hard to correlate the experimental results in the literature as band alignment, band bending, and charge carrier profiles were often not determined on the same samples.

It must thus be stated that a conclusive band scheme of the LaAlO₃/SrTiO₃ heterojunction is yet to be derived. For this purpose we have revisited this system by the most comprehensive and systematic approach applied so far. Using angle-resolved HAXPES and Poisson-Schrödinger modeling, we achieve unprecedented sensitivity and reliability in our analysis and derive the charge carrier distribution as well as the valence band edge profile self-consistently from the same

TABLE I. Band bending and alignment at the epitaxial (001)-oriented LaAlO₃/SrTiO₃ heterointerface as determined by various photoemission studies. (a) Tentative sketch of the band profile. The figure is not drawn to scale but is defining the variables used in (b) and (c). Valence band offset ΔE_{VB} (b) and estimates for the depth of the confining potential and 2DES extension in SrTiO₃ (c) by different groups.

(a)		(b) Valence band offset		
		Publication	ΔE_{VB} (eV)	Sample fully oxidized
	Susaki <i>et al.</i> [22]	+0.42	yes	
	Berner <i>et al.</i> [25]	+0.36	yes	
	Chambers <i>et al.</i> [26] (Augsburg sample)	+0.2	yes	
	Qiao <i>et al.</i> [23,24]	+0.16	yes	
	Yoshimatsu <i>et al.</i> [32]	0.0	yes	
	Treske <i>et al.</i> [30]	0.0	no	
	Chambers <i>et al.</i> [26] (Tokyo sample)	-0.06	no	
	Drera <i>et al.</i> [27]	-0.1	no	
	Segal <i>et al.</i> [28]	-0.35	yes	
	(c) Potential profile and 2DES extension in SrTiO ₃			
Publication	ΔE_{BB} (eV)	d_{BB} (Å)	Sample fully oxidized	
Berner <i>et al.</i> [25]	0 ± 0.3	-	yes	
Yoshimatsu <i>et al.</i> [32]	0.25 ± 0.07	-	yes	
Chambers <i>et al.</i> [26] (Augsburg sample)	0 ± 0.06	-	yes	
Drera <i>et al.</i> [29]	0.8 ± 0.2	-	no	
Treske <i>et al.</i> [30]	≥ 0.4	≥ 20	no	
Chambers <i>et al.</i> [26] (Tokyo sample)	0 ± 0.06	-	no	
Publication		d_{2DES} (Å)	Sample fully oxidized	
Sing <i>et al.</i> [33] (Augsburg samples)		4-40	yes	
Slooten <i>et al.</i> [34] (good substrate)		≥ 80	yes	
Sing <i>et al.</i> [33] (PSI sample)		4-12	no	
Slooten <i>et al.</i> [33] (bad substrate)		25 ± 15	no	

sample. By means of synchrotron light irradiation and simultaneous oxygen dosing, we are additionally capable of varying the oxygen vacancy (V_O) concentration in the LaAlO₃/SrTiO₃ sample [31] in a controlled way. This allows us to derive a complete band diagram of the heterostructure dependent on the oxidation state. Based on this thorough analysis we identify the doping level of mobile charge carriers as the crucial parameter determining the band alignment scheme, thereby resolving many of the existing inconsistencies in the literature. We furthermore elucidate the vital role, which the dielectric permittivity of SrTiO₃ and in particular, its dependence on the electric field plays in determining the interfacial electronic properties.

Our results are of general relevance to layered oxide architectures, in which often materials with different oxygen affinities and high dielectric permittivities are combined.

The paper is organized as follows: The experimental methods are described in Sec. II. In Sec. III, the angle-dependent substrate core level spectra are analyzed. Employing the Poisson-Schrödinger equation we derive the band profile and charge distribution in the SrTiO₃ substrate. The interfacial band alignment is scrutinized in Sec. IV, followed by an evaluation of the potential build up in the LaAlO₃ film in Sec. V. In Sec. VI we contrast our results to the earlier publications and conclude our study in Sec. VII.

II. EXPERIMENT

LaAlO₃/SrTiO₃ heterostructures were fabricated by pulsed laser deposition. The LaAlO₃ films were deposited on undoped, TiO₂-terminated, (001)-oriented SrTiO₃ substrates at an oxygen partial pressure of 1×10^{-3} mbar, a substrate temperature of 780°C, and a laser fluence of 1.1 J/cm². Reflection high-energy electron diffraction was used to monitor the film growth *in situ*. After growth the samples were slowly cooled down to room temperature in 500 mbar O₂ with the temperature being held constant at 600°C. In transport experiments a metal-insulator transition was observed at a LaAlO₃ film thickness of 4 unit cells (uc), consistent with the critical thickness reported in the literature [7,35]. The samples were then removed from the growth vessel and transported to the synchrotron. Photoemission was measured at Beamline I09 at Diamond Light Source on a 4 uc-LaAlO₃/SrTiO₃ heterostructure at 60 K without further surface treatment. The conducting interface was grounded by several Al wire bonds penetrating through the film into the substrate and with their other ends connected to the sample carrier. No charging was observed. For the photoemission measurements of the bare substrate, Nb-doped SrTiO₃ was used to prevent charging.

In a previous study we demonstrated that we can control the oxygen stoichiometry and thus the doping level of the

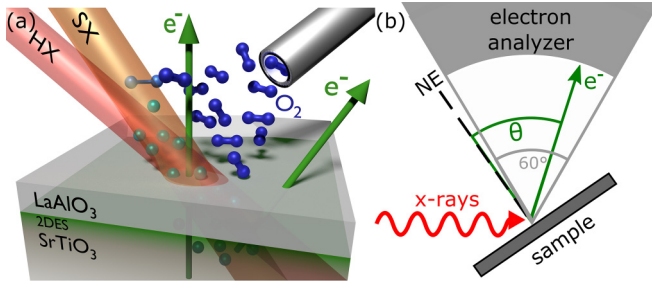


FIG. 1. (a) Setup of the photoemission experiment. By a combination of O dosing and the intense x-ray irradiation we can precisely control the oxygen stoichiometry in the heterostructure during the photoemission experiment. The probing depth of the photoelectrons varies with their emission angle. (b) Making use of a wide angle acceptance lens photoelectrons emitted at an angle of 5° – 65° with respect to the sample surface normal can be recorded by the analyzer simultaneously. In consequence, the depth distribution of the photoelectrons can be probed without changing the measurement geometry.

LaAlO₃/SrTiO₃ heterointerface with a combination of x-ray irradiation and *in situ* dosing of molecular oxygen [31]. An artistic view of this setup is shown in Fig. 1(a).

The oxygen vacancy concentration in the SrTiO₃ substrate is monitored by recording valence band spectra with soft x-rays as described in Ref. [31]. Two distinct Ti 3*d*-related features are known to appear in the valence band spectra of oxygen depleted SrTiO₃, a metallic quasiparticle (QP) peak at the Fermi energy [cf. Fig. 2(a)] and a broad structure in the gap (IG) at about 1.3 eV binding energy [cf. Fig. 2(b)], reflecting localized states induced by oxygen vacancies [36–40]. These Ti 3*d*-related states cannot be detected at high photon energies due to the minute Ti 3*d* photoemission cross sections. Tuning the photon energy across the Ti *L* edge at around 460 eV allows the Ti 3*d* photoemission signal to be resonantly enhanced and thus enables the observation of the QP and IG features of a LaAlO₃/SrTiO₃ heterostructure [41,42]. Note that the resonance energies for the QP and IG states differ by 1 eV.

The soft x-ray beam and the 3 keV x-ray beam are focused to the same spot on the sample [see illustration in Fig. 1(a)]. We are thus able to prepare a sample state, assess the oxygen

vacancy concentration on the basis of the IG and QP weights in the soft x-ray valence band spectra and subsequently record core level spectra of the very same sample spot and oxidation state with the enhanced probing depth of the 3 keV hard x-ray beam, which is appropriate for characterizing the band edge profiles of both the LaAlO₃ film and the SrTiO₃ substrate.

In our experiment we probe two different oxidation states of the 4 uc-LaAlO₃/SrTiO₃ sample. We investigate the *fully oxidized state*, which is measured under full oxygen dosing such that all oxygen vacancies in the SrTiO₃ substrate are quenched and the heterointerface is exclusively doped by electronic reconstruction. This can be seen in the soft x-ray valence band spectra displayed in Figs. 2(a) and 2(b) in blue: Even at the IG resonance the IG feature is completely suppressed [Fig. 2(b)], but yet finite QP weight is observed at the QP resonance energy [Fig. 2(a)], which is ascribed to mobile electrons induced by the electronic reconstruction [31]. The *oxygen depleted state* is, in contrast, prepared by x-ray irradiation without oxygen dosing until the V_O concentration has saturated, as can be monitored by the saturation of the IG feature in the valence band spectra measured at IG resonance [see red spectrum in Fig. 2(b)]. At the QP resonance the QP feature increases as well under oxygen depletion [see red spectrum in Fig. 2(a)], which proves that the charge carrier concentration in the 2DES can be tuned by the oxygen stoichiometry.

For depth profiling of the band bending and the charge carriers, we record spectra at different electron emission angles with a Scienta EW4000 analyser. When an electron from a given depth is emitted at an angle θ with respect to the surface normal, its path to the surface is elongated by the factor $\frac{1}{\cos(\theta)}$ and the probing depth of the measurement decreases accordingly by $\cos(\theta)$. The wide angle lens of the analyzer allows us to simultaneously collect electrons emitted over a range from 5° to 65° with respect to the sample surface normal, which is evenly divided into five slices. The measurement geometry is sketched in Fig. 1(b). In this way we are able to record five angle-dependent spectra within a 60° -window in a single shot and, in particular, in the same measurement geometry. To calibrate the binding energy scale over the full angular range, the Fermi edge of Au was measured in the same angular mode.

To analyze the core level spectra a Shirley background is subtracted while for the Sr 3*d* spectra the additional contributions of La 4*d* and Sr 3*d* satellite peaks are corrected for.

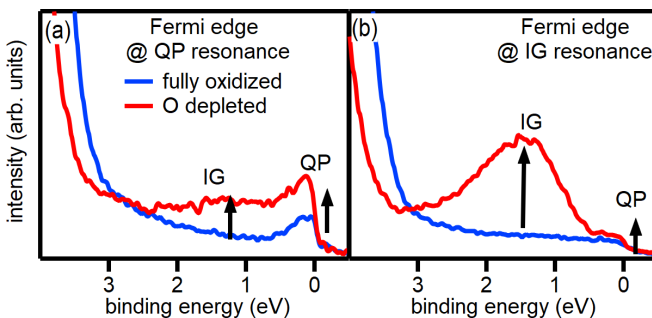


FIG. 2. Valence band spectra of the fully oxidized (blue lines) and the oxygen depleted state (red lines) of a LaAlO₃/SrTiO₃ heterostructure recorded with soft x-rays at the QP (a) and the IG resonance (b).

III. HAXPES DEPTH PROFILING OF 2DES

To investigate the band bending and charge carrier distribution in the SrTiO₃ substrate we probe the electron emission angle dependence of the Ti 2*p* and Sr 3*d* spectra measured at 3 keV.

We first turn to the spectra in the fully oxidized state [Fig. 3(a)]: Compared to the corresponding spectra of the SrTiO₃ substrate (dashed gray lines) the Ti 2*p* and Sr 3*d* HAXPES spectra of the fully oxidized LaAlO₃/SrTiO₃ heterostructure are slightly shifted and broadened towards the high binding energy side. The broadening in the core level lines increases with the electron emission angles, i.e., the sensitivity to the interface [marked by arrows in Fig. 3(a)]. The observed asymmetries and shifts are ascribed to a *downward*

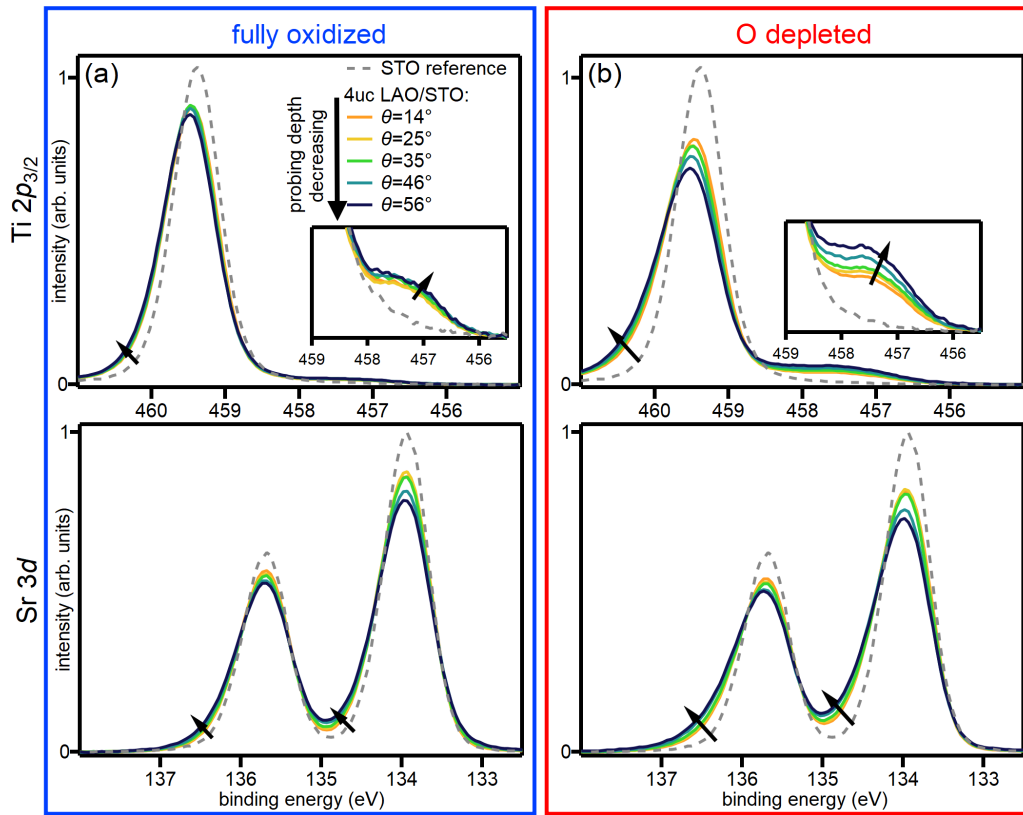


FIG. 3. Electron emission angle dependence of substrate core level spectra for a 4 uc $\text{LaAlO}_3/\text{SrTiO}_3$ heterostructure. $\text{Ti } 2p$ (top) and $\text{Sr } 3d$ (bottom) spectra of the sample in the fully oxidized (a) and oxygen depleted (b) state.

band bending on the SrTiO_3 side towards the interface, which shifts the photoemission signals originating at a depth closer to the interface more towards a higher binding energy.

Note that the electron-emission-angle dependent broadening of the $\text{Sr } 3d$ spectra has been claimed to be induced by Sr segregation on the LaAlO_3 film surface [43]. With additional experimental evidence we show, in the Supplemental Material [44], that our samples do not exhibit Sr segregation.

In the $\text{Ti } 2p$ spectra of the $\text{LaAlO}_3/\text{SrTiO}_3$ heterostructure we observe an additional peak, which appears at a lower binding energy (see insets in Fig. 3). This peak is noticeably absent in the $\text{Ti } 2p$ spectra of the fully oxidized SrTiO_3 substrate (see dashed lines in Fig. 3). The main line and the lower binding energy component in the $\text{Ti } 2p$ spectra can be attributed to Ti ions with valences of 4+ and 3+, i.e., electron configurations of $3d^0$ and $3d^1$, respectively [33]. This observation of finite Ti^{3+} weight matches the finite QP weight detected in the soft x-ray valence band spectra of the fully oxidized heterostructure [see Fig. 2(a)] [31]. The Ti^{3+} spectral weight in the $\text{Ti } 2p$ spectra of the $\text{LaAlO}_3/\text{SrTiO}_3$ heterostructure only shows a slight dependence on the electron emission angle.

Next we focus on the spectra recorded in the O depleted state [Fig. 3(b)]. The broadening and shifts of the $\text{Sr } 3d$ and $\text{Ti } 2p$ core level lines are now more pronounced than in the fully oxidized state [see arrows in Figs. 3 (b)]. Furthermore, the Ti^{3+} weight has noticeably increased. In particular, the asymmetries in the core level main lines and the enhanced Ti^{3+} weights now vary more strongly with the electron emission angle [see insets of Figs. 3(a) and 3(b)].

Based on these observations, we can obtain a qualitative understanding of the band scheme in the two oxidation states. The binding energies of the core level lines as well as the $\text{Ti } 3d$ occupation vary more considerably on the scale of the photoemission probing depth in the oxygen depleted state than in the fully oxidized state. We infer that the SrTiO_3 bands are more strongly bent downward near the interface and that the 2DES is more closely confined to the $\text{LaAlO}_3/\text{SrTiO}_3$ interface under oxygen depletion than full oxidation. For a quantitative account of the band bending, we model the data based on the Poisson-Schrödinger equation.

A. Poisson-Schrödinger method

Photoemission studies are often exploited to extract either the charge carrier profiles [33,34,47] or the band profiles in heterostructures [25,48–51]. In some publications [48] both quantities are determined but still treated by separate approaches and fitted using *independent* models. For instance, to determine the charge carrier distribution in SrTiO_3 -based heterostructures, the dependence of the Ti^{3+} weight on the electron emission angle has been analyzed assuming a homogeneous distribution of the mobile electrons [33,34,47,48]. However, if the overall Ti^{3+} weight is small—as is the case for fully oxidized samples—the subtle variations in the Ti^{3+} weight with the electron emission angle can result in large errors in determining the 2DES extension.

Here, we combine the analysis of the charge carrier distribution and the band bending to improve the reliability and

accuracy in deriving both quantities. To ensure the physical links between these two quantities, we model them with functions, which solve Poisson's and Schrödinger's equations *self-consistently* [52–60].

We assume that the charge carrier distribution and the band bending varies only in the direction perpendicular to the interface (z direction). Thus, Poisson's equation reads

$$\frac{\partial}{\partial z} \left(\epsilon_r \epsilon_0 \frac{\partial \Phi(z)}{\partial z} \right) = -e(N_D(z) - n(z)), \quad (1)$$

where $\Phi(z)$ describes the electrostatic potential and $n(z)$ denotes the concentration of mobile electrons. ϵ_0 stands for the vacuum permittivity while ϵ_r denotes the dielectric constant of the SrTiO₃ substrate. If there are *ionized* donors present in the system, their concentration $N_D(z)$ enters Poisson's equation as well.

The one-dimensional Schrödinger equation reads

$$\left(-\frac{\hbar^2}{2m^*} \frac{\partial^2}{\partial z^2} - e\Phi(z) \right) \Psi_l(z) = E_l \Psi_l(z), \quad (2)$$

where m^* denotes the effective mass of the electrons and $\Psi_l(z)$ and $E_l(z)$ denote the eigenfunction and corresponding eigenenergy, respectively, labeled by the subband index l . To calculate the charge carrier density profile $n(z)$, we sum up the probability densities $\Psi_l^*(z)\Psi_l(z)$ of the states of each subband

$$n(z) = \sum_l \Psi_l^*(z)\Psi_l(z)n_l \quad (3)$$

weighted by their occupation probabilities n_l

$$n_l = \frac{bm^*}{\pi \hbar^2} \int_{E_l}^{\infty} \frac{1}{1 + e^{(E_B - E_l)/k_B T}} dE_B, \quad (4)$$

where b denotes the number of degenerate bands. The ‘‘1D Poisson’’ program written by G. Snider [54,55,61] is employed to find the self-consistent solutions to Poisson's and Schrödinger's equations.

B. Modeling SrTiO₃ based heterostructures

Next we apply the Poisson-Schrödinger approach to the LaAlO₃/SrTiO₃ heterostructures. The electrostatic potential $\Phi(z)$ is linked to the conduction band profile $E_c(z)$ in the LaAlO₃/SrTiO₃ heterostructure by $E_c(z) = -e\Phi(z)$. The LaAlO₃ film is treated as an infinite potential barrier to prevent charge carriers from leaking into the LaAlO₃ film. Figure 4 illustrates how the different doping mechanisms in SrTiO₃ in the heterostructures are modelled in the Poisson-Schrödinger method. The figure shows the respective distributions of mobile charge carriers $n(z)$ (dashed lines) and of ionized donors $N_D(z)$ (solid lines).

In the case of electronic reconstruction (blue panel in Fig. 4), there are no oxygen vacancies, i.e., no ionized donor atoms in the SrTiO₃ substrate itself. $N_D(z)$ is consequently set to zero except at the very interface ($z = 0$). There, an infinite layer of positive charges is introduced, which is needed to compensate for the mobile charge carrier density n_{er} that results from the electronic reconstruction [62].

When SrTiO₃ is exclusively doped by electrons released from oxygen vacancies (gray panel in Fig. 4), the

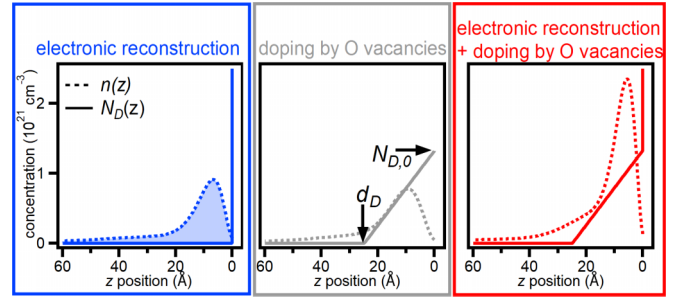


FIG. 4. Poisson-Schrödinger approach for different kinds of doping. 3D concentration of mobile charge carriers (dashed lines) and of ionized donors (solid lines). Blue: Doping by electronic reconstruction for fully oxidized epitaxial LaAlO₃/SrTiO₃ samples. Gray: Doping by oxygen vacancies for, e.g., disordered LaAlO₃/SrTiO₃ samples. Red: Combination of doping by oxygen vacancies and electronic reconstruction for oxygen depleted epitaxial LaAlO₃/SrTiO₃ samples.

infinitesimally thin layer of positive charges at $z = 0$ is removed. According to Ref. [63], we assume that one of the two electrons released by each oxygen vacancy remains localized while the other electron is mobile. An oxygen vacancy thus effectively carries a single positive charge. The oxygen vacancies can consequently be treated as if they were *singly ionized* dopant atoms in the conventional semiconductor picture and enter in Poisson's equation (1) as the term $N_D(z)$. In the ensuing fits we assume that the oxygen vacancy concentration peaks at the interface and decreases linearly into the SrTiO₃ bulk [solid line in Fig. 4(b)]. The V_O profile is described by two parameters, the V_O concentration $N_{D,0}$ at the interface and the thickness d_D of the V_O -doped layer.

In oxygen depleted epitaxial LaAlO₃/SrTiO₃ heterostructures we observe a combination of these two doping mechanisms. In this case both the infinitesimally thin layer of positive charges and the linearly z dependent V_O concentration are included in $N_D(z)$.

To keep our fit model simple, we settle for working with a single isotropic effective mass m^* describing the electrons in the three Ti $3d t_{2g}$ orbitals. Consequently, the number b of degenerate bands is set to three.

C. Peculiarities of the SrTiO₃ dielectric constant

The *static* dielectric constant ϵ_r dictates the polarization of the bound charges that arises from and counteracts a built-in electric field [64]. In LaAlO₃/SrTiO₃ heterostructures electronic reconstruction and oxygen vacancies lead to a distribution of positive charges and an electric field in the SrTiO₃ near the interface, to which the bound and mobile charges in the SrTiO₃ substrate react. ϵ_r is thus an essential parameter determining the distribution of mobile electrons $n(z)$ and the confining potential $\Phi(z)$. In the limit of high ϵ_r throughout the SrTiO₃ substrate, the polarization of bound charges largely compensates the built-in electric field, bringing about a shallow potential well and a mobile charge carrier distribution, which could extend far into the SrTiO₃ bulk. A smaller ϵ_r should therefore lead to a steeper potential well and mobile electrons more confined to the interface region.

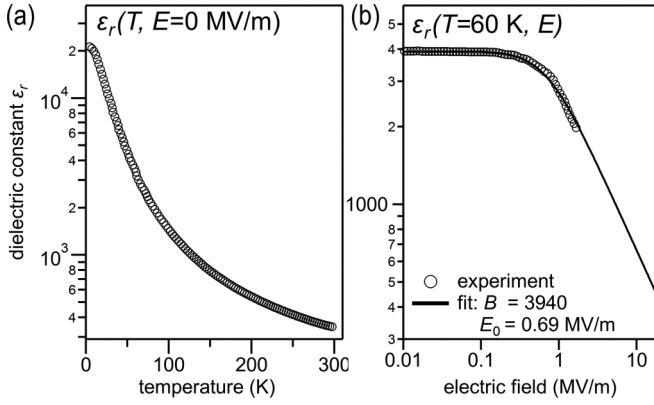


FIG. 5. (a) Temperature dependence of the dielectric constant of a (001)-oriented SrTiO₃ single crystal [65]. (b) Electric field dependence of the dielectric constant of single-crystal SrTiO₃ at $T = 60$ K. Experimental data from Ref. [66]. Data fitted according to (5).

Being a quantum paraelectric, ϵ_r of SrTiO₃ can be very large but is *strongly dependent* on the temperature and the electric field as shown in Figs. 5(a) [65] and 5(b) [66], respectively. To take into account the latter dependence we introduce a z -dependent ϵ_r , which changes as a function of the electric field $E(z)$ as described by the empirical formula proposed by Fête *et al.* [65,67] as

$$\epsilon_r(E) = 1 + \frac{B}{[1 + (E/E_0)^2]^{1/3}}. \quad (5)$$

$B + 1$ and E_0 describe the dielectric constant at zero field and the electric field beyond which ϵ_r starts to decrease noticeably, respectively.

From the SrTiO₃ bulk towards the interface the electrostatic field generated by the positive charges near the interface increases substantially. Consequently, the dielectric response and thus the field compensation weakens towards the interface as ϵ_r of SrTiO₃ decreases rapidly with increasing electric field. As a result, the net electric field strength varies more steeply with z and yields a potential well of stronger confinement. Once trapped in the potential well, the mobile electrons in turn screen the positive charges at the interface, reduce their impact on the band profile away from the interface and further sharpen the charge carrier distribution. The important role of this field dependence of ϵ_r in sharpening the depth distribution of the 2DES at the LaAlO₃/SrTiO₃ interface has been demonstrated by previous simulations [68].

D. Layer-resolved Ti 2p and Sr 3d spectra

To outline how the functions $n(z)$, $N_D(z)$, and $\Phi(z)$ enter into the fit models of the core level data, we consider the analysis of a Ti 2p spectrum. It is made up of the contributions originating from the individual TiO₂ layers as exemplarily illustrated in Fig. 6, where for clarity only the top eight layers are shown. Yet, layers situated up to 200 Å into the SrTiO₃ substrate are included in our models. Thereby, we capture virtually all ($\geq 99\%$) of the Ti 2p photoelectrons, which escape from the SrTiO₃ substrate.

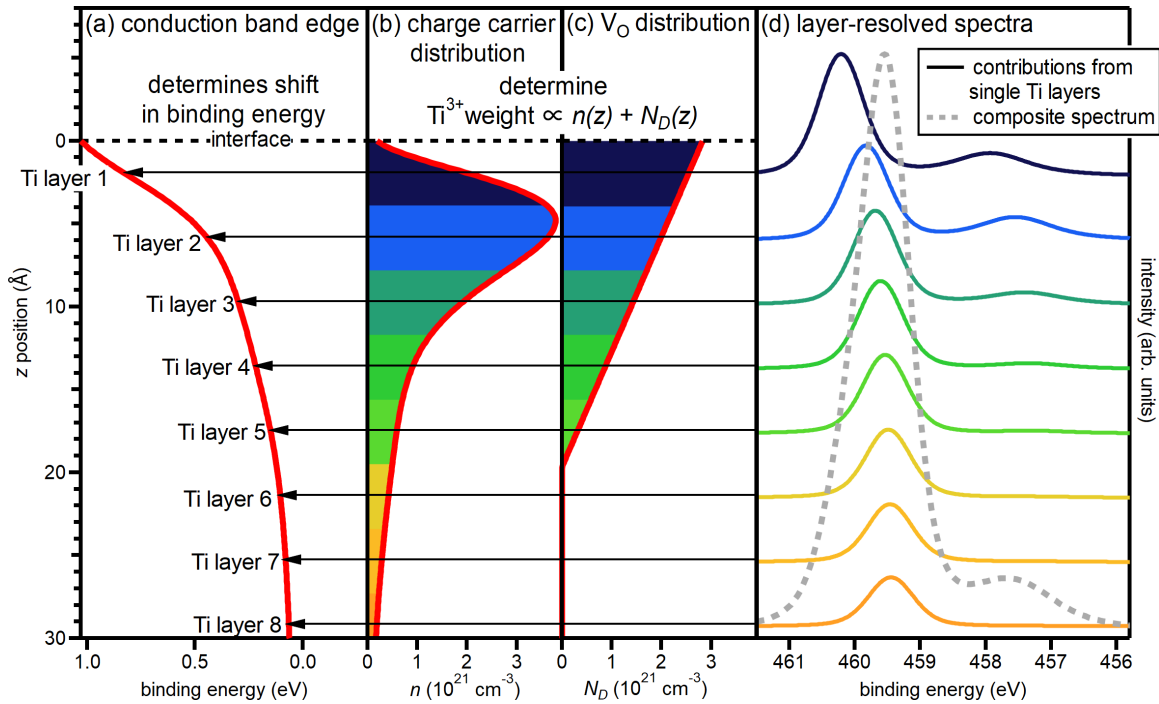


FIG. 6. Layer-resolved composition of an exemplary Ti 2p spectrum. (a) Conduction band profile near the interface. (b) Concentration of mobile electrons. (c) Concentration of trapped electrons (corresponding to the concentration of oxygen vacancies). (d) Ti 2p spectra of the first eight TiO₂ layers. The binding energy of the single spectra is determined by the interfacial band bending at position z [see arrows in (a)]. The Ti³⁺ weight of the single spectra is proportional to the sum of the mobile and trapped charge carrier concentration, which is integrated over the corresponding unit cell [see colored intervals in (b) and (c)].

For each layer-resolved spectrum [see colored lines in Fig. 6(d)], we model the 4+ and 3+ components of the Ti $2p_{3/2}$ peak each with a Voigt profile. The spectral shapes of the two components and the energy separation between them are shared across all layers, whereas the binding energies of the Ti $2p$ core level lines are allowed to change across the layers to reflect the binding energy shifts of the conduction band edge at the respective depths z from the interface [see arrows in Fig. 6(a)]. All mobile electrons [Fig. 6(b)], i.e., the electrons released by the electronic reconstruction and by oxygen vacancies [Fig. 6(c)], contribute to the Ti^{3+} weight in the layer-resolved spectra. Furthermore, each oxygen vacancy does not only release one mobile electron but also one electron trapped in the $3d$ shell at a neighboring Ti site, which consequently also contributes to the Ti^{3+} weight. The Ti^{3+} signal originating from a TiO_2 layer at depth z is thus proportional to $\int_{z-\frac{a}{2}}^{z+\frac{a}{2}} d\tilde{z}(n(\tilde{z}) + N_D(\tilde{z}))$ where a denotes the SrTiO_3 lattice constant. In each of the layer-resolved Ti $2p$ spectra, the Ti^{4+} weight is diminished by the Ti^{3+} weight present in that spectrum. To account for the attenuation of the outgoing photoelectrons, the signal originating from a TiO_2 layer at depth z is exponentially damped by the factor $e^{-z/\lambda_{\text{IMFP,Ti}2p} \cos \theta}$ where θ describes the photoelectron emission angle with respect to the surface normal and $\lambda_{\text{IMFP,Ti}2p}$ denotes the inelastic mean free path of the Ti $2p$ photoelectrons [69]. We model the Sr $3d$ spectra in a similar fashion [73].

E. Global fitting scheme

For each oxidation state (fully oxidized and oxygen depleted) we measured the Sr $3d$ and Ti $2p$ core levels at five different electron emission angles, i.e., probing depths, yielding twenty spectra in total to fit. To obtain reliable fits, we reduce the number of fitting parameters by applying the same Poisson-Schrödinger parameters m^* , B , and E_0 to model all spectra, independent of the electron emission angle, core level, or oxidation state [74]. We assume that the polarisability of oxygen-deficient STO is comparable to stoichiometric SrTiO_3 . Considering also the fact that the maximum V_O concentration in our heterostructures is on the order of only 10 at.%, we can safely ignore the dependence of ϵ_r of SrTiO_3 on the V_O concentration to simplify our model. The electronic reconstruction is furthermore assumed to provide the same total number n_{er} of mobile charge carriers independent of the oxidation state, i.e., the same infinitesimally thin layer of positive charge at the interface is applied to all twenty spectra. To describe the oxygen deficient state, we only need to introduce in addition a V_O profile governed by $N_{D,0}$ and d_D . We apply similar constraints to the fitting parameters defining the Voigt functions for the core levels. We then model the twenty spectra *all at once* in a *global fit* involving in total 21 *independent* fitting parameters, which amounts to ≈ 1 independent parameter per spectrum.

F. Discussion of fit results

Figure 7 compares the measured Ti $2p$ and Sr $3d$ core level spectra with their best fits for the fully oxidized (blue panel) and the O depleted (red panel) states at the maximal and minimal electron emission angles. The fits reproduce the

prominent features and trends in the spectra: The variations in the Ti^{3+} weights and in the Ti^{3+} and Sr $3d$ line shapes with electron emission angle are accurately captured.

To check whether the fits to the heterostructure data are physically meaningful, we compare the above results with those obtained from fitting the Ti $2p_{3/2}$ and Sr $3d$ spectra of the fully oxidized substrate [see Fig. 3, grey dashed lines]. Here, each individual peak can be modeled with a single Voigt profile (not shown), indicating that the pristine SrTiO_3 barely exhibits any band bending. Thus, we view these spectra as reference spectra of SrTiO_3 . We find that the fitting parameters deduced from the $\text{LaAlO}_3/\text{SrTiO}_3$ heterostructure and the SrTiO_3 reference for the Ti $2p_{3/2}$ and Sr $3d$ core levels are very similar and also agree well with the typical values reported in literature [29,33,48].

The resulting fitting parameters appearing in Poisson's and Schrödinger's equations are listed in Table II for the two $\text{LaAlO}_3/\text{SrTiO}_3$ oxidation states. The derived B and E_0 match the values expected in the temperature range of 60–80 K [Fig. 5(b)]. The fitted value for the effective isotropic mass $0.84m_e$ is in good agreement with the estimations from fully relativistic band-structure calculations by Marques *et al.* [75], $m^* = 0.8m_e$, and specific-heat measurements by Okuda *et al.* [76], $m^* = 1.17m_e$. The mobile charge carrier concentration n_{er} of the fully oxidized state is in the same order of magnitude as the one obtained in transport experiments on the fully oxidized sample. Note that the oxygen depleted state is confined to the spot on which the x-ray beam impinges and thus cannot be easily isolated and probed in transport experiments.

G. The electrostatics at the $\text{LaAlO}_3/\text{SrTiO}_3$ interface

The conduction band profiles resulting from our fitting routine are depicted in Fig. 8(c) together with the energy levels of the corresponding subbands for each case. In both the fully oxidized (blue lines) and the O depleted (red lines) states the conduction bands are bent downward toward the interface, creating a potential well in which the mobile electrons accumulate. The band bending at the interface is more pronounced in the oxygen depleted than in the fully oxidized state, which is brought about by the additional interface dipole induced by the oxygen vacancies. For numerical reasons, a slightly n -doped SrTiO_3 substrate was assumed in the Poisson-Schrödinger model fits leading to a pinning of the Fermi level at the conduction band minimum in the bulk of SrTiO_3 . Note, however, that with the assumed slight background doping the three-dimensional charge density of bulk SrTiO_3 is several orders of magnitude lower than that of the interface 2DES and below the percolation threshold [77].

Figure 8(a) depicts the distributions of the mobile electrons $n(z)$ for the two states. The total concentration of mobile charge carriers is considerably higher in the O depleted state as mobile electrons are released by oxygen vacancies in addition to the electronic reconstruction.

Furthermore, the mobile charge carrier concentration is strongly confined and peaks close to the interface for both states. To compare the spatial extension of the mobile charge carriers, we normalize the charge carrier profiles to the respective total concentration of mobile charge carriers Q_{total} [see Fig. 8(b)]. We find that the 2DES is slightly more extended

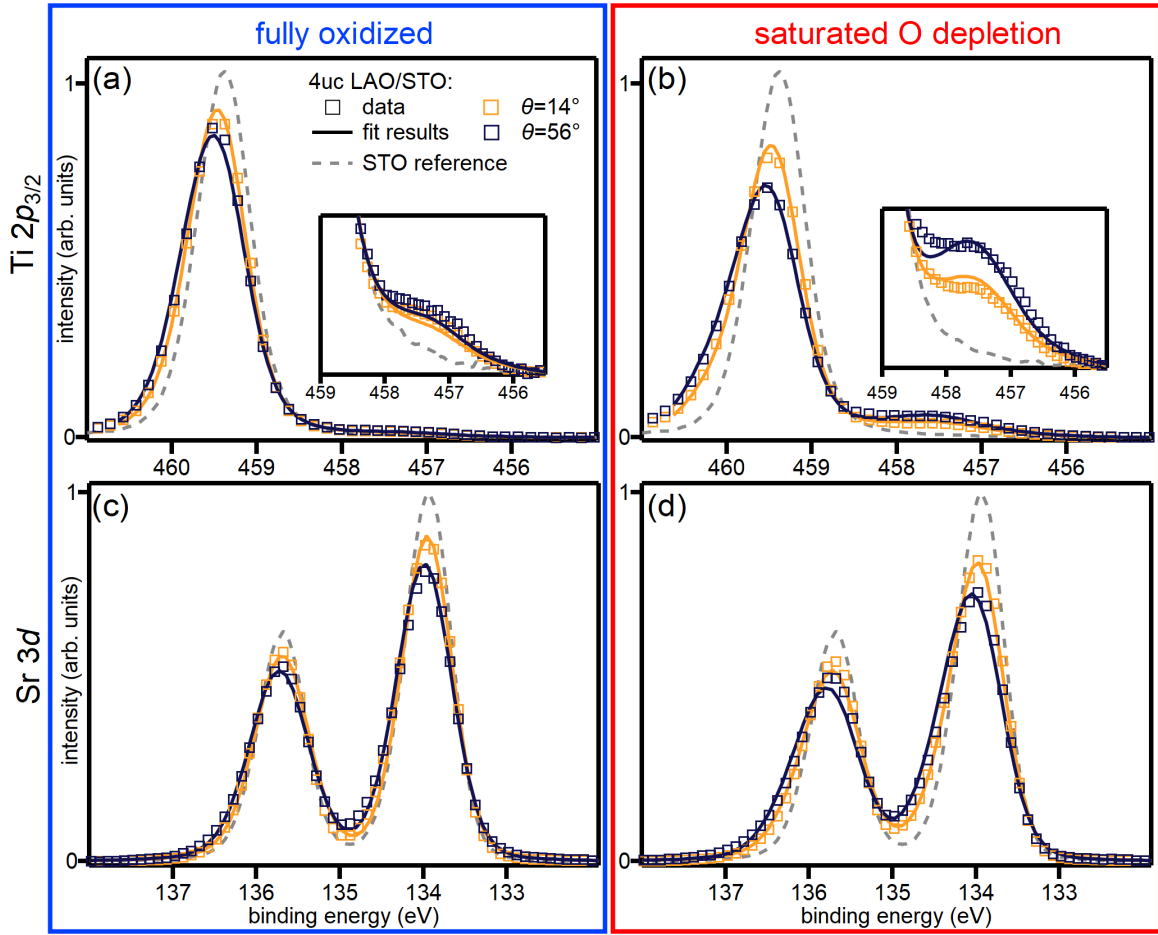


FIG. 7. Fits of Ti $2p$ and Sr $3d$ core level spectra with the Poisson-Schrödinger method. A comparison between the Ti $2p$ spectra at the extremal electron emission angles and the corresponding fits is shown in (a) and (b) for the fully oxidized and the O depleted state, respectively. Corresponding figures for the Sr $3d$ core level are shown in (c) and (d). The fitted curves agree well with the measured data. SrTiO₃ reference spectra are shown for comparison.

in the fully oxidized state than in the O depleted state. The maximum of the charge carrier distribution in the fully oxidized state undergoes a small shift of 2.5 Å into the SrTiO₃ bulk, with additionally a tail extending further into the SrTiO₃ substrate [see arrow in Fig. 8(b)], which is not present in the oxygen depleted state. Oxygen depletion thus increases strongly the charge carrier concentration and further sharpens slightly the depth distribution.

The characteristic profile of the charge carrier concentration develops as a result of the electric field dependence of ϵ_r . In Figs. 8(d) and 8(e) the z dependencies of the electric

field and ϵ_r , respectively, are depicted for the two oxidation states. Deep in the SrTiO₃ substrate the electric fields are small and do not differ very much between the two states [see dashed ellipse in Fig. 8(d)] as the charges induced by electronic reconstruction and oxygen vacancies are expected to reside close to the interface. Accordingly, the dielectric constant ϵ_r in the SrTiO₃ bulk adopts high and similar values in both states [see dashed ellipse in Fig. 8(e)]. Toward the interface the electric field increases strongly in both states leading to a substantial decrease in ϵ_r [see solid ellipses in Figs. 8(d) and 8(e)]. In the vicinity of the interface, ϵ_r falls to

TABLE II. Fit results of the Poisson-Schrödinger model for a (001)-oriented LaAlO₃/SrTiO₃ heterostructure. We specify the best-fit values as well as error margins.

	Fit parameters applicable to both oxidation states				V_0 profile O depleted state	
	$n_{\text{er}} (10^{14} \text{ cm}^{-2})$	$m^* (m_e)$	B	$E_0 (\text{MV/m})$	$N_{D,0} (10^{21} \text{ cm}^{-3})$	$d_D (\text{Å})$
Best fit	1.66	0.84	3 400	0.95	2.83	19.8
Lower limit	1.46	0.73	2 930	0.76	2.23	15.3
Upper limit	1.91	1.02	3 880	1.17	3.48	23.3

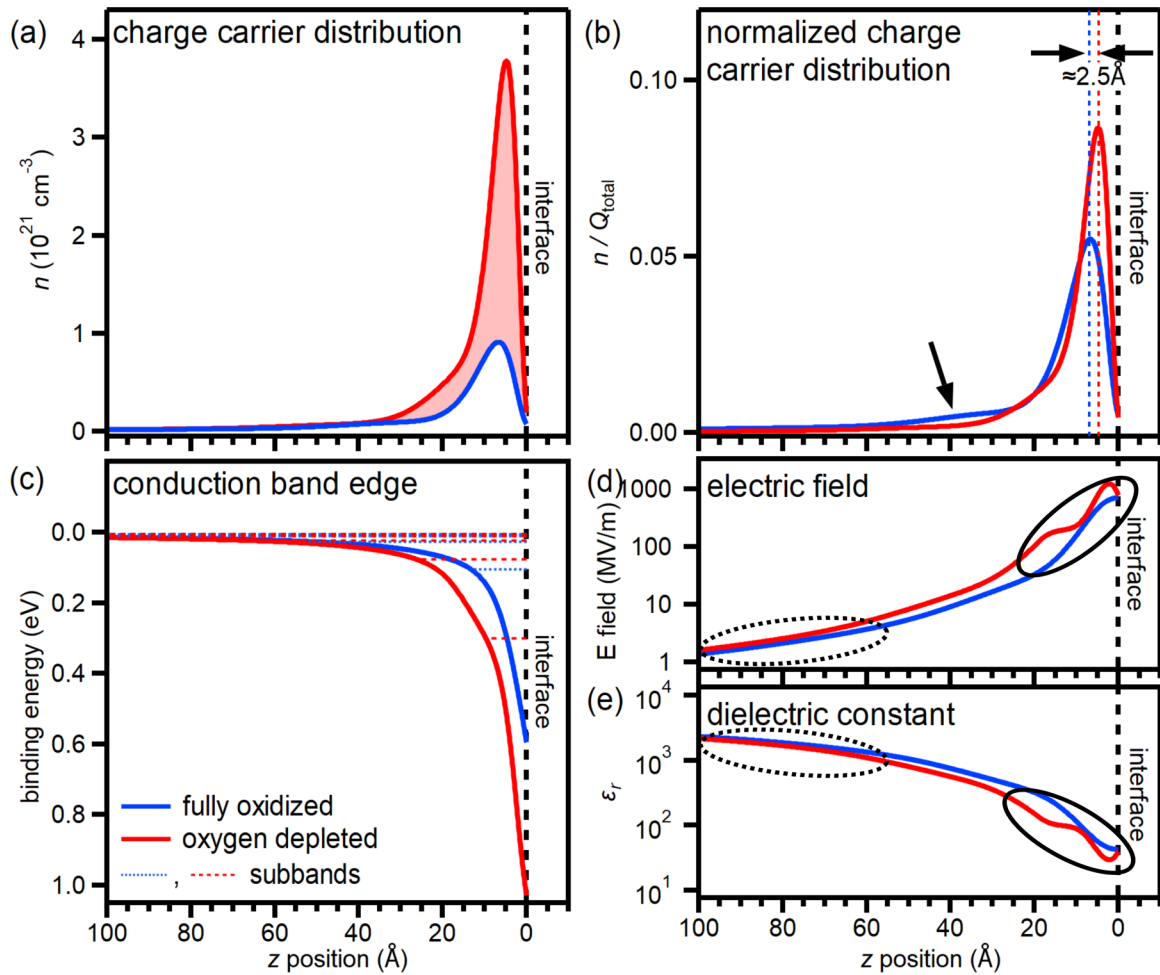


FIG. 8. The electrostatics at the (001)-oriented LaAlO₃/SrTiO₃ heterostructure in the fully oxidized and the oxygen depleted state. (a) Distribution of the mobile charge carriers. (b) Distribution of the mobile charge carriers normalized by the total mobile charge carrier concentration Q_{total} . (c) Conduction band profile with subband structure. The Fermi energy is pinned at the conduction band minimum in the bulk of SrTiO₃. (d) Profile of the electric field. (e) Profile of the dielectric constant. For details see text.

only 40 – 70, allowing a strong confinement of the electron system to the interface, as discussed in Sec. III C. As the z dependence of ϵ_r is overall similar in both states, the depth extension of the 2DES depends only weakly on the oxygen stoichiometry.

A closer look at Fig. 8(d) shows that the electric field is always slightly higher in the O depleted state. This is induced by the oxygen vacancies, which are charged and increase the electric field, leading to a smaller ϵ_r near the interface. In consequence, the mobile charge carriers are slightly more confined to the interface and the band bending is more pronounced in the O depleted state than in the fully oxidized state.

IV. THE INTERFACIAL BAND ALIGNMENT

We now turn to the band alignment at the LaAlO₃/SrTiO₃ interface, which is derived both from the core level and from the valence band spectra.

A. Core level analysis

Angle-integrated HAXPES spectra comprising the film core levels La 4*d* and Al 2*s* as well as the substrate core level Sr 3*d* are depicted in Fig. 9. Depending on the oxidation state, the binding energies of the film core levels clearly vary.

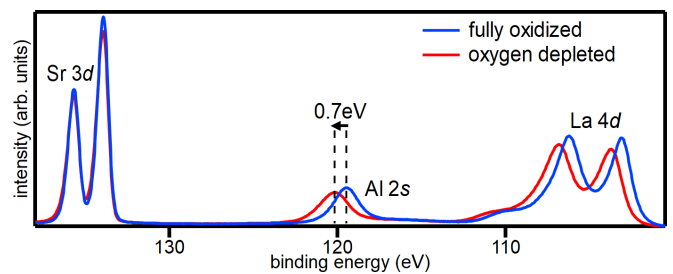


FIG. 9. Angle-integrated spectra comprising the Sr 3*d*, Al 2*s*, and La 4*d* core levels of a LaAlO₃/SrTiO₃ heterostructure in the fully oxidized and the O depleted state. As a function of the oxygen stoichiometry we observe a pronounced shift in the film core level binding energies.

TABLE III. Valence band offsets at the (001) LaAlO₃/SrTiO₃ heterointerface in the fully oxidized and the O depleted state from core level and valence band analyses.

Analysis method	Fully oxidized	O depleted
Core level analysis	(+0.14 ± 0.2) eV	(−0.58 ± 0.2) eV
Valence band analysis	(+0.13 ± 0.2) eV	(−0.43 ± 0.2) eV

Since a similar binding energy shift occurs also to the LaAlO₃ valence band maximum, these shifts are likely to arise from the interfacial band alignment that depends on the V_O concentration.

Within the flat band scenario the valence band offset across the LaAlO₃/SrTiO₃ interface can be determined quantitatively by analyzing the binding energy differences between selected core levels and the valence band maxima (VBM) in LaAlO₃ and SrTiO₃ reference samples [78], and in the LaAlO₃/SrTiO₃ heterostructure as [79]

$$\Delta E_{\text{VB}} = (E_{\text{Sr}3d_{5/2}} - E_{\text{VBM}})_{\text{STO}} - (E_{\text{Al}2s} - E_{\text{VBM}})_{\text{LAO}} - (E_{\text{Sr}3d_{5/2}} - E_{\text{Al}2s})_{\text{LAO/STO}}$$

where $(E_x)_y$ denotes the binding energy of spectral feature x of compound y . The valence band offsets estimated by this method are shown in the top row of Table III.

B. Valence band analysis

The valence band offsets can also be determined based solely on the HAXPES valence band spectra, where that of the heterostructure is a weighted superposition of those from the LaAlO₃ film and the SrTiO₃ substrate. Figure 10(a) depicts the valence band spectra of the LaAlO₃/SrTiO₃ heterostructure in the two different states, which exhibits a clear offset between the band edges, confirming that the band alignment changes with the V_O concentration. For comparison, we also show in the inset valence band spectra of bare SrTiO₃ in the fully oxidized and the oxygen depleted state, normalized by acquisition time and photon flux. Note, however, that the oxygen depleted state differs from that of the SrTiO₃ substrate in the heterostructure by the (larger) amount and distribution of oxygen vacancies and hence the band bending. Nonetheless, it is also interesting to remark that from the ratio of the total valence band spectral weights the oxygen loss is estimated to be less than 2%, fully consistent with the result of the same analysis of the corresponding O 1s core level spectra (see Supplemental Material [44]).

To determine the actual band offsets in the heterostructure, the valence band spectra are decomposed into the film and substrate contributions by a fitting scheme. Due to the band bending in the SrTiO₃ substrate we have to model the SrTiO₃ contribution layer-by-layer as in the previous section, namely, each SrTiO₃ layer's contribution is represented by a reference valence band spectrum of SrTiO₃ shifted in energy according to the band edge profile derived above and damped by an exponential factor corresponding to its depth below the surface. Assuming a flat band picture, we then add as the LaAlO₃ contribution a reference LaAlO₃ valence band spectrum for each LaAlO₃ layer, which is shifted in binding energy to

account for the band offset at the interface and also damped. To reduce the number of fitting parameters, we once again fit the valence band spectra of both states simultaneously and only allow the binding energy of the LaAlO₃ valence band to vary depending on the oxidation state.

The fitted and measured valence band spectra are compared in Figs. 10(b) and 10(c) for the oxygen depleted and the fully oxidized states, respectively. The resulting LaAlO₃ and SrTiO₃ contributions are shown as well. The thus estimated valence band offsets are listed in the bottom row of Table III.

C. The resulting band diagram

Table III shows that the two methods described above yield similar results for the two oxidation states. The sign of the valence band offset changes between the fully oxidized and oxygen depleted states, as can be seen in Figs. 10(b) and 10(c) with the valence band edge of the LaAlO₃ moving from below to above that of the SrTiO₃. This sign change reveals that the LaAlO₃/SrTiO₃ heterojunction switches its character from a staggered (type II interface) to a straddling gap arrangement (type I interface) with an increasing V_O concentration. Figure 11 depicts the band diagram as inferred from our analysis. Both the LaAlO₃ and SrTiO₃ band edges at the interface are found to shift towards higher binding energy upon reduction of the interface (see arrows in Fig. 11). The shifts of the band edges are furthermore of similar magnitudes, suggesting that the LaAlO₃ and SrTiO₃ band edges are locked to each other at the interface and shifted together by the interface dipole, which depends on the V_O concentration. This observation is consistent with the mechanism proposed by Zhong and Hansmann [80] that band alignment across an oxide/oxide heterointerface is mostly achieved via the alignment of the two O 2p bands, which fixes the band offset at the interface.

We also put our band diagram to test by analyzing the O 1s spectra, which also contain contributions from both the film and the substrate, using the method described for the valence band in Sec. IV B. The result is found to corroborate the band diagram in Fig. 11 (see Fig. S10 in Supplemental Material for details [44]).

V. THE POTENTIAL PROFILE IN THE LaAlO₃ FILM

The earlier explanations for the formation of the 2DES at the LaAlO₃/SrTiO₃ interface referred to a diverging potential in the LaAlO₃ film increasing with the film thickness [81]. However, previous photoemission experiments have failed to confirm this scenario and, instead, found ubiquitous flat-bands across the LaAlO₃ film [25–30,34,82].

To look for a potential gradient in the LaAlO₃ overlayer, we compare the line shapes of the angle-integrated Al 1s and La 4d spectra between the fully oxidized and oxygen depleted states in Fig. 12(a) after aligning the corresponding spectra in binding energy. We note that we have to use slightly different binding energy shifts to align the core level spectra for Al 1s and La 4d [see annotations in Fig. 12(a)], the reason of which will become clearer soon. The Al 1s and the La 4d spectra are found to undergo similar broadening in the O depleted

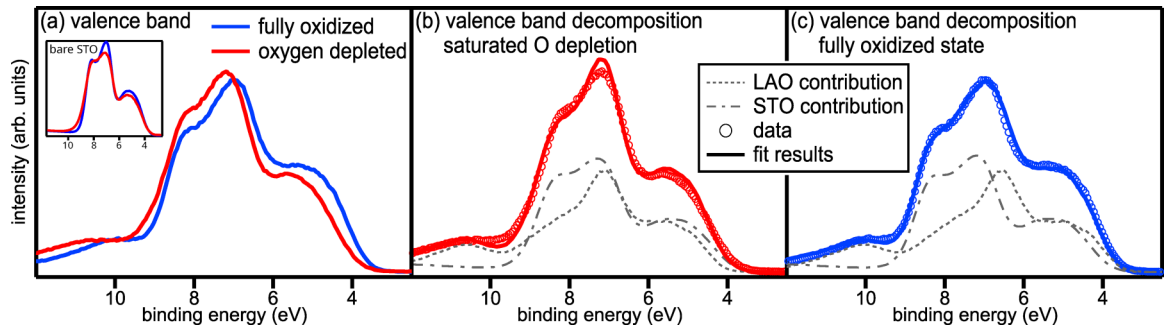


FIG. 10. (a) Valence band spectra of the $\text{LaAlO}_3/\text{SrTiO}_3$ heterostructure for the fully oxidized and the oxygen depleted state. The spectral shape as well as the onset of the valence band spectrum changes as a function of the oxygen stoichiometry. Inset: Valence band spectra of bare SrTiO_3 for the fully oxidized and the oxygen depleted state. [(b),(c)] Measured data, fit and decomposition of the valence band spectra into the LaAlO_3 and SrTiO_3 contributions in the oxygen depleted and in the fully oxidized state, respectively. The LaAlO_3 valence band contribution (dotted line) clearly shifts in binding energy as a function of the V_{O} concentration.

state, consistent with a change of the potential profile across the LaAlO_3 film.

A. Extracting the potential profile in the LaAlO_3 film

In Fig. 12(b) we plot the binding energy shifts of the maxima of the $\text{Al } 1s$ and $\text{La } 4d_{5/2}$ core level spectra versus the electron emission angles. Note that we plot the binding energy shifts over all electron emission angles recorded. For each core level, the average binding energy for the fully oxidized state is chosen as the reference. The analysis in Fig. 12(b) confirms that the binding energies depend on the oxidation state.

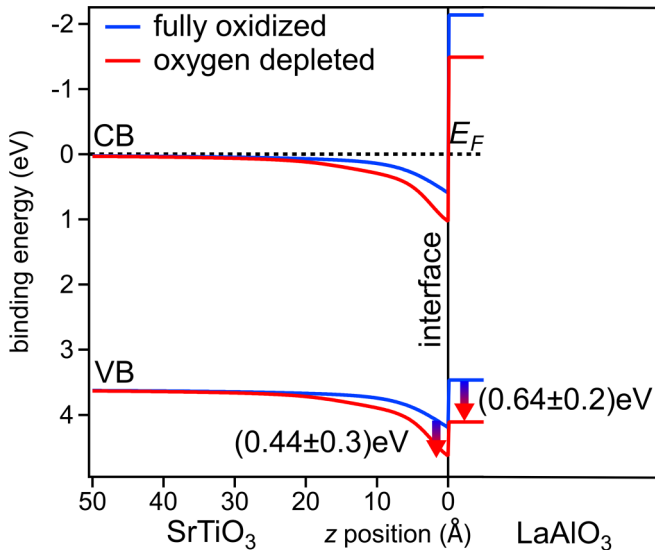


FIG. 11. Band diagram of the (001)-oriented $\text{LaAlO}_3/\text{SrTiO}_3$ heterostructure in the fully oxidized and O depleted state. The offset between the valence band edges of LaAlO_3 and SrTiO_3 right at the interface is fixed independent of the oxidation state. The change in the valence band offset is calculated from averaged values in Table III, the change in the potential well depth is read out from Fig. 8(c). The Fermi energy is pinned at the conduction band minimum in the bulk of SrTiO_3 (see Sec. III G).

It furthermore shows that in the fully oxidized state the binding energy does not vary with the emission angle, suggesting flat bands in the LaAlO_3 film. While this observation contradicts the simple electronic reconstruction picture [83], a plausible explanation of this discrepancy is available from a modified scenario in which oxygen vacancies at the LaAlO_3 surface act as the charge reservoir for the electronic reconstruction [34,41,84]. Above the critical thickness these defect states form as their formation enthalpy is exceeded by the energy gain from donating electrons to the interface, resulting in a dipole field that counteracts the potential build-up in the polar LaAlO_3 film [84–88].

In contrast, Fig. 12(b) shows that in the oxygen depleted state the binding energy does vary as a function of the electron emission angle, explaining the broadening observed in the angle-integrated $\text{Al } 1s$ and $\text{La } 4d$ core level spectra [see Fig. 12(a)] and providing evidence for a potential build-up in the LaAlO_3 film in this state. As the film core levels shift to higher binding energies at larger electron emission angles, the bands are bent downward toward the film surface. Note that, besides this overall trend, the core level binding energies display additional small modulations with the emission angle. This is ascribed to x-ray photoelectron diffraction (XPD), as explained in the Supplemental Material [44]. In the following analysis we thus focus on the angle-integrated data in which these effects are averaged out.

Since bending of the LAO band edges is only observed under oxygen depletion, it stands to reason that beam-induced, charged oxygen vacancies can form not only in the SrTiO_3 substrate but also in the LaAlO_3 film and give rise to the potential drop toward the LaAlO_3 film surface.

To give a more quantitative account of this band bending, we model the angle-integrated $\text{Al } 1s$ and $\text{La } 4d_{5/2}$ spectra of the O depleted state with reference spectra as before. Since flat band behavior is observed in the fully oxidized state, we use the spectra measured under oxygen dosing [see blue spectra in Fig. 12(a)] as reference spectra to describe the $\text{Al } 1s$ and $\text{La } 4d$ signals originating from the individual AlO_2 and LaO layers in the LaAlO_3 film. Layer-dependent binding energy shifts are applied to the reference spectra to account for the band bending and allowed to vary to best reproduce the measured spectra. To constrain the fit, we require the

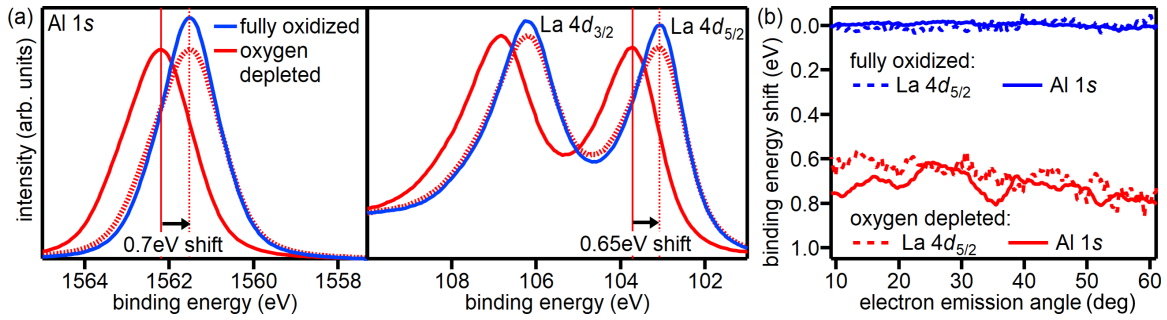


FIG. 12. Analyzing the core level spectra of the LaAlO_3 film. (a) Angle-integrated Al $1s$ and La $4d$ spectra. As a function of the oxidation state there is not only a shift in binding energy but also a change of the spectral shape. (b) Binding energy of the Al $1s$ and La $4d_{5/2}$ core level maxima dependent on the electron emission angle. For each core level, binding energies are referenced to the average binding energies in the fully oxidized state.

potential to change monotonically across the LaAlO_3 film. Note that this procedure automatically includes the interfacial band alignment as a fit parameter. Figure 13(a) shows that the thus modeled angle-integrated La $4d$ and Al $1s$ spectra can well reproduce the measured ones for the oxygen depleted state. The potential profile the best fit yields is displayed in Fig. 13(b) as red squares, which shows a sizable drop toward the LaAlO_3 surface. In Fig. 13(b) the dotted and solid lines mark where the potential is read out for the LaO and AlO_2 layers, respectively. As the potential changes continuously across the LaAlO_3 film, the potential at the AlO_2 and the LaO layers of the same unit cell can differ. This difference is reflected in the 50 meV difference in the binding energy shifts between the Al $1s$ and La $4d$ spectra under oxygen depletion [see Fig. 12(a)].

B. Refining the band diagram

In Sec. IV C we put forward a band diagram of the $\text{LaAlO}_3/\text{SrTiO}_3$ heterointerface in the fully oxidized and the O depleted state, assuming that the bands in the LaAlO_3 are flat. This overestimates the valence band offset in the oxygen depleted state as the bands in the LaAlO_3 film are found to be actually bent downward. Taking into account the valence band edge profiles in the LaAlO_3 film for the oxygen depleted state

from the previous section [see Fig. 13(b)], we refine our band diagram and plot the result in Fig. 14.

We find that the band edge shift of SrTiO_3 at the interface between the two sample states now matches even better to that of the LaAlO_3 (see arrows in Fig. 14), which corroborates our hypothesis that the band alignment right at the interface is fixed, independent of the V_{O} concentration.

The finding that the potential build-up in the LaAlO_3 film in the O depleted state is induced by positively charged oxygen vacancies in the LaAlO_3 film raises the question of the whereabouts of the electrons, which are released by the oxygen vacancies. Just as the oxygen vacancies at the LaAlO_3 surface are suggested to act as a charge reservoir for the 2DES in the fully oxidized state [84], the oxygen vacancies forming in the LaAlO_3 film under O depletion could supply additional mobile electrons to the interfacial 2DES. To simulate such a scenario, we would have to modify our Poisson-Schrödinger model as upon oxygen depletion mobile charge carriers are not only released by oxygen vacancies in the SrTiO_3 substrate but also by those in the LaAlO_3 film. Since such a model would contain too many unknown parameters, we will not pursue this idea further. However, the general findings of the simulations will not change as only the charge reservoirs providing mobile electrons would differ.

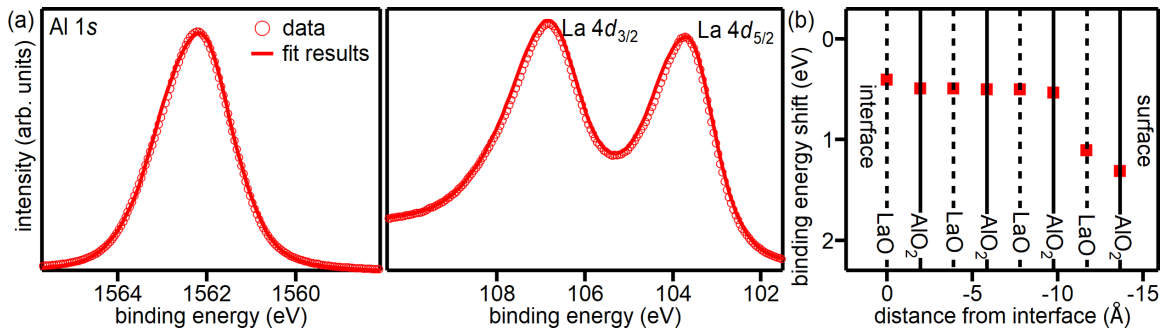


FIG. 13. Modeling the potential profile in the LaAlO_3 film in the oxygen depleted state. (a) Fits of the angle-integrated Al $1s$ (left) and La $4d$ (right) spectra. The fitted curves agree well with the measured data. (b) Resulting potential profile. The binding energy shifts show the difference in binding energy between the oxygen depleted state and the fully oxidized state.

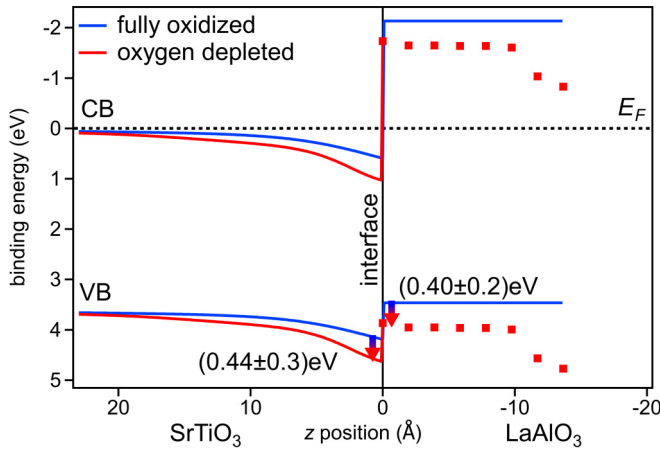


FIG. 14. Refined band diagram of the (001)-oriented $\text{LaAlO}_3/\text{SrTiO}_3$ heterostructure in the fully oxidized and oxygen depleted state. The arrows indicate the changes in the band offsets at both sides of the interface upon O depletion. The Fermi energy is pinned at the conduction band minimum in the bulk of SrTiO_3 (see Sec. III G).

VI. DISCUSSION AND COMPARISON TO PREVIOUS PHOTOEMISSION STUDIES

In the preceding sections we analyzed the band diagram in epitaxial $\text{LaAlO}_3/\text{SrTiO}_3$ heterostructures at different oxidation states, i.e., at different doping levels. Next we will revisit the earlier photoemission studies and try to reconcile their inconsistencies with the systematics of our results. Table IV lists the results of our analysis, while the outcomes of earlier photoemission studies are summarized in Table I [89]. As the oxidation state has proven to be an essential parameter, we also indicate in Table I whether the sample was fully oxidized or oxygen depleted [90]. Note that O depleted samples can be obtained from x-ray exposure or prepared by PLD growth under O poor conditions. However, this difference can be ignored as the relevant parameter is the doping level, which can be controlled by both preparation methods.

We observed a change in the oxygen stoichiometry driven by the intense focused hard x-ray beam. This effect has not been reported in the publications referenced in Table I, which can probably be ascribed to a lower photon flux in these experiments, most of which are run in a laboratory XPS setup or at bending magnet beamlines. The Ti $2p$ reference spectra of SrTiO_3 substrates included in some of these publications [22,25,29,30,32,34] do furthermore not show any Ti^{3+} weight, confirming that the irradiation does not create oxygen vacan-

TABLE IV. Synopsis of the results of the HAXPES depth profiling experiments at the (001)-oriented $\text{LaAlO}_3/\text{SrTiO}_3$ heterostructure: valence band offset ΔE_{VB} , energy depth ΔE_{BB} , and spatial width d_{BB} of the potential well in the SrTiO_3 substrate and 2DES extension $d_{2\text{DES}}$ in the fully oxidized and the O depleted state.

	ΔE_{VB} (eV)	ΔE_{BB} (eV)	d_{BB} (Å)	$d_{2\text{DES}}$ (Å)
Fully oxidized	$+0.13 \pm 0.20$	0.46 ± 0.10	26 ± 5	37 ± 4
Oxygen depleted	-0.58 ± 0.20	0.82 ± 0.10	22 ± 3	20 ± 2

cies in these experiments. For the publications in Table I the irradiation of the sample can be neglected, while the oxidation state set by the growth remains essential.

A. The band profile in the SrTiO_3 substrate

To compare our SrTiO_3 band profiles to the results in earlier publications, we define the depth ΔE_{BB} of the potential trough to be the binding energy difference of the valence band edge between the STO at the interface and in the bulk, and the width d_{BB} of the potential well to be the distance from the interface to where the band bending decreases to 10% of ΔE_{BB} .

We find that ΔE_{BB} is about 0.5 eV for the fully oxidized state and rises up to about 0.8 eV under oxygen depletion (see Fig. 14 and Table IV). The results of most photoemission studies are in line with these findings [cf. Table I(c)], i.e., studies investigating fully oxidized samples only detect small or even no band bending in the SrTiO_3 substrate, while nearly all publications analyzing oxygen depleted samples find evidence for a deep potential trough at the $\text{LaAlO}_3/\text{SrTiO}_3$ interface. However, the exact values of ΔE_{BB} differ in our analysis and the previous publications. In the case of the oxygen depleted state, this discrepancy can be ascribed to the differing V_{O} concentration and distribution, which impacts the interface dipole and thus the band profile in the SrTiO_3 . Similarly, the surface preparation can change the band profile in the SrTiO_3 substrate, as it dictates the amount of adsorbates at the LaAlO_3 surface, which are known to be able to dope charge carriers into the interfacial 2DES and, in turn, change the potential trough on the SrTiO_3 side of the interface [91,92]. The modulations in the potential trough in the fully oxidized state can similarly be attributed to the different mobile charge carrier concentrations, which may either be induced by growth conditions or by the surface preparation. In addition, the absence of a potential well reported in some of the earlier photoemission studies may also be ascribed to insufficient resolution to resolve the shallow potential well.

B. The band alignment at the $\text{LaAlO}_3/\text{SrTiO}_3$ heterointerface

Our results for the interfacial valence band offsets ΔE_{VB} (see Table IV) reveal that the band alignment changes from a staggered gap configuration in the fully oxidized state to a straddling gap configuration in the oxygen depleted state. Note that, to facilitate the comparison with the literature, the values of ΔE_{VB} in Table IV are indicated as determined within a flat band scenario, which was assumed by most previous studies. Broadly consistent with our finding, Table I(b) shows mostly positive values of ΔE_{VB} for earlier studies on samples that were fully oxidized and negative values for those that were not. The remaining variations in the valence band offset among the oxygen depleted samples and among the fully oxidized samples can be attributed to the differences in the V_{O} concentration and the number of mobile charge carriers, which are likely induced by the differences in the growth conditions or the surface preparation. It has been reported that the valence band offset does vary with the surface preparation [26,92].

There is one notable exception regarding the valence band offsets in Table I(b): Segal *et al.* [28] investigated a sample, which was annealed in flowing oxygen at 350°C to quench all oxygen vacancies created during the deposition process. Yet, the negative valence band offset they find from a core-level analysis is reminiscent of an oxygen depleted sample. This might be due to the annealing temperature being too low to fill up all oxygen vacancies in the LaAlO₃/SrTiO₃ heterostructure or a pronounced variation in the cation stoichiometry of the LaAlO₃ film [26,82]. Note that the sample investigated by Segal *et al.* is the only sample in Table I(b), which is not fabricated by PLD but by molecular beam epitaxy (MBE).

C. The potential build-up in the LaAlO₃ film

In agreement with the earlier publications we do not find any evidence for a potential gradient in the LaAlO₃ film in the fully oxidized LaAlO₃/SrTiO₃ heterostructure [26–30,34,41,82].

In contrast, for the O depleted state we have observed a downward band bending in the LaAlO₃ film induced by charged oxygen vacancies in the LaAlO₃ film. Tracking core level peak positions as a function of the LAO thickness, Segal *et al.* [28] also detected a potential gradient in the LaAlO₃ film in heterostructures, which are oxygen-depleted during growth. They find a gradient of the *same sign* as in our sample but with a smaller magnitude. The differences in the magnitude of the potential gradient might be due to the different amounts and distributions of oxygen vacancies in the LaAlO₃ film.

D. The 2DES extension

To compare our quantitative results to the results of earlier publications for the 2DES extension, we define the 2DES extension d_{2DES} in our analysis as the average distance of the mobile electrons from the interface (see Table IV). Although most of the mobile electrons are narrowly confined to the interface in both oxidation states, d_{2DES} is larger in the fully oxidized than in the O depleted state, mainly due to the tail of electrons reaching in the SrTiO₃ substrate in the fully oxidized state. The strong confinement of the mobile electrons is induced by the electric field dependent dielectric constant $\epsilon_r(E)$ of SrTiO₃. The decisive role of $\epsilon_r(E)$ in determining the charge carrier distribution in LaAlO₃/SrTiO₃ heterostructures has also been found in conductive-tip atomic force microscopy probing the 2DES extension [93].

The values reported in earlier photoemission studies for the 2DES extension [see Table I(d)] scatter strongly and have

large error bars, in particular in the case of fully oxidized samples [33,34]. We ascribe the diverse findings in the literature to the difficulty in analyzing the angle-dependence of a weak Ti³⁺ shoulder. With our much more sophisticated approach, which fits the band bending and the charge carrier distribution simultaneously, we are able to estimate the 2DES extension more reliably.

VII. CONCLUSIONS

Although the band bending and the band alignment at the epitaxial LaAlO₃/SrTiO₃ heterointerface has already been investigated in numerous photoemission studies, a conclusive band diagram has not emerged to date. In this paper we thus revisit the topic and investigate the electronic interface properties with hard x-ray photoemission. As the doping in the sample varies with an increasing oxygen vacancy concentration, the SrTiO₃ and LaAlO₃ bands are found to change concurrently to keep the band offset constant at the interface, resulting in a crossover of the band alignment from a type II to a type I interface. The mobile charge carriers are furthermore shown to accumulate near the interface in both oxidation states with a minor tail extending much deeper into the substrate in the fully oxidized state. The dielectric constant of SrTiO₃ with its intricate dependence on the electric field proves to be the crucial parameter inducing the charge carrier confinement. In the LaAlO₃ film, we find a downward band bending for samples prepared with a high concentration of beam-induced V_O, while a flat-band behavior is observed for fully oxidized samples. Based on these findings, we show that most of the inconsistencies in earlier photoemission studies can be reconciled. Our insights into the band engineering at LaAlO₃/SrTiO₃ heterointerfaces may prove useful for future device applications where precise control of the interfacial electronic properties such as the band alignment and band edge profile are essential.

ACKNOWLEDGMENTS

The authors are grateful for financial support from the Deutsche Forschungsgemeinschaft (DFG, German Research Foundation) through the Collaborative Research Center SFB 1170 ToCoTronics (Project I.D. 258499086) and the Würzburg-Dresden Cluster of Excellence on Complexity and Topology in Quantum Matter-ct.qmat (EXC 2147, Project I.D. 390858490) and acknowledge Diamond Light Source for time on beamline I09 under Proposals No. SI11394, No. SI12044, and No. SI14432. The authors also thank D. McCue for his superb technical support at the I09 beamline.

-
- [1] J. Heber, Materials science: Enter the oxides, *Nature (London)* **459**, 28 (2009).
 [2] A. Ohtomo and H. Y. Hwang, A high-mobility electron gas at the LaAlO₃/SrTiO₃ heterointerface, *Nature (London)* **427**, 423 (2004).
 [3] A. Brinkman, M. Huijben, M. van Zalk, J. Huijben, U. Zeitler, J. C. Maan, W. G. van der Wiel, G. Rijnders, D. H. A. Blank, and H. Hilgenkamp, Magnetic effects at the

interface between non-magnetic oxides, *Nat. Mater.* **6**, 493 (2007).

- [4] S. J. Callori, J. Gabel, D. Su, J. Sinsheimer, M. V. Fernandez-Serra, and M. Dawber, Ferroelectric PbTiO₃/SrRuO₃ Superlattices with Broken Inversion Symmetry, *Phys. Rev. Lett.* **109**, 067601 (2012).
 [5] A. D. Caviglia, M. Gabay, S. Gariglio, N. Reyren, C. Cancellieri, and J.-M. Triscone, Tunable Rashba Spin-Orbit

- Interaction at Oxide Interfaces, *Phys. Rev. Lett.* **104**, 126803 (2010).
- [6] N. Reyren, S. Thiel, A. D. Caviglia, L. F. Kourkoutis, G. Hammerl, C. Richter, C. W. Schneider, T. Kopp, A.-S. Rüetschi, D. Jaccard *et al.*, Superconducting interfaces between insulating oxides, *Science* **317**, 1196 (2007).
- [7] S. Thiel, G. Hammerl, A. Schmehl, C. W. Schneider, and J. Mannhart, Tunable quasi-two-dimensional electron gases in oxide heterostructures, *Science* **313**, 1942 (2006).
- [8] B. Förg, C. Richter, and J. Mannhart, Field-effect devices utilizing LaAlO₃-SrTiO₃ interfaces, *Appl. Phys. Lett.* **100**, 053506 (2012).
- [9] P. Maier, F. Hartmann, J. Gabel, M. Frank, S. Kuhn, P. Scheiderer, B. Leikert, M. Sing, L. Worschech, R. Claessen, and S. Höfling, Gate-tunable, normally-on to normally-off memristance transition in patterned LaAlO₃/SrTiO₃ interfaces, *Appl. Phys. Lett.* **110**, 093506 (2017).
- [10] K. Miller, F. Hartmann, B. Leikert, S. Kuhn, J. Gabel, M. Sing, R. Claessen, and S. Höfling, Room temperature memristive switching in nano-patterned LaAlO₃/SrTiO₃ wires with laterally defined gates, *Appl. Phys. Lett.* **118**, 153502 (2021).
- [11] E. Lesne, Y. Fu, S. Oyarzun, J. C. Rojas-Sánchez, D. C. Vaz, H. Naganuma, G. Sicoli, J.-P. Attané, M. Jamet, E. Jacquet *et al.*, Highly efficient and tunable spin-to-charge conversion through Rashba coupling at oxide interfaces, *Nat. Mater.* **15**, 1261 (2016).
- [12] Q. Song, H. Zhang, T. Su, W. Yuan, Y. Chen, W. Xing, J. Shi, J. Sun, and W. Han, Observation of inverse Edelstein effect in Rashba-split 2DEG between SrTiO₃ and LaAlO₃ at room temperature, *Sci. Adv.* **3**, e1602312 (2017).
- [13] A. Chaves, J. G. Azadani, H. Alsalmán, D. R. da Costa, R. Frisenda, A. J. Chaves, S. H. Song, Y. D. Kim, D. He, J. Zhou, *et al.*, Bandgap engineering of two-dimensional semiconductor materials, *npj 2D Mater. Appl.* **4**, 29 (2020).
- [14] H. Kroemer, Nobel Lecture: Quasielectric fields and band offsets: Teaching electrons new tricks, *Rev. Mod. Phys.* **73**, 783 (2001).
- [15] S. A. Chambers, M. Chrysler, J. H. Ngai, T.-L. Lee, J. Gabel, B. E. Matthews, S. R. Spurgeon, M. E. Bowden, Z. Zhu, and P. V. Sushko, Mapping hidden space-charge distributions across crystalline metal oxide/group IV semiconductor interfaces, *Phys. Rev. Mater.* **6**, 015002 (2022).
- [16] C. Franchini, Hybrid functionals applied to perovskites, *J. Phys.: Condens. Matter* **26**, 253202 (2014).
- [17] J. Gabel, M. Pickem, P. Scheiderer, L. Dudy, B. Leikert, M. Fuchs, M. Stübinger, M. Schmitt, J. Küspert, G. Sangiovanni *et al.*, Toward functionalized ultrathin oxide films: The impact of surface apical oxygen, *Adv. Electron. Mater.* **8**, 2101006 (2022).
- [18] K. A. Müller and H. Burkard, SrTiO₃: An intrinsic quantum paraelectric below 4 K, *Phys. Rev. B* **19**, 3593 (1979).
- [19] O. Aktas, S. Crossley, M. A. Carpenter, and E. K. H. Salje, Polar correlations and defect-induced ferroelectricity in cryogenic KTaO₃, *Phys. Rev. B* **90**, 165309 (2014).
- [20] S. A. Chambers, L. Wang, and D. R. Baer, Introductory guide to the application of XPS to epitaxial films and heterostructures, *J. Vac. Sci. Technol. A* **38**, 061201 (2020).
- [21] A. Giampietri, G. Drera, and L. Sangaletti, Band alignment at heteroepitaxial perovskite oxide interfaces. Experiments, methods, and perspectives, *Adv. Mater. Interfaces* **4**, 1700144 (2017).
- [22] T. Susaki, S. Ueda, K. Matsuzaki, T. Kobayashi, Y. Toda, and H. Hosono, Photoemission study of LaAlO₃/SrTiO₃ and LaAlO₃/Nb:SrTiO₃: Insulator-insulator versus insulator-semiconductor interfaces, *Phys. Rev. B* **94**, 075311 (2016).
- [23] L. Qiao, T. Droubay, V. Shutthanandan, Z. Zhu, P. Sushko, and S. Chambers, Thermodynamic instability at the stoichiometric LaAlO₃/SrTiO₃ (001) interface, *J. Phys.: Condens. Matter* **22**, 312201 (2010).
- [24] L. Qiao, T. C. Droubay, T. C. Kaspar, P. V. Sushko, and S. A. Chambers, Cation mixing, band offsets and electric fields at LaAlO₃/SrTiO₃(001) heterojunctions with variable La:Al atom ratio, *Surf. Sci.* **605**, 1381 (2011).
- [25] G. Berner, A. Müller, F. Pfaff, J. Walde, C. Richter, J. Mannhart, S. Thiess, A. Gloskovskii, W. Drube, M. Sing, and R. Claessen, Band alignment in LaAlO₃/SrTiO₃ oxide heterostructures inferred from hard x-ray photoelectron spectroscopy, *Phys. Rev. B* **88**, 115111 (2013).
- [26] S. A. Chambers, M. H. Engelhard, V. Shutthanandan, Z. Zhu, T. C. Droubay, L. Qiao, P. V. Sushko, T. Feng, H. Lee, T. Gustafsson, E. Garfunkel, A. B. Shah, J.-M. Zuo, and Q. M. Ramasse, Instability, intermixing and electronic structure at the epitaxial heterojunction, *Surf. Sci. Rep.* **65**, 317 (2010).
- [27] G. Drera, G. Salvinelli, F. Bondino, E. Magnano, M. Huijben, A. Brinkman, and L. Sangaletti, Intrinsic origin of interface states and band-offset profiling of nanostructured LaAlO₃/SrTiO₃ heterojunctions probed by element-specific resonant spectroscopies, *Phys. Rev. B* **90**, 035124 (2014).
- [28] Y. Segal, J. H. Ngai, J. W. Reiner, F. J. Walker, and C. H. Ahn, X-ray photoemission studies of the metal-insulator transition in LaAlO₃/SrTiO₃ structures grown by molecular beam epitaxy, *Phys. Rev. B* **80**, 241107(R) (2009).
- [29] G. Drera, G. Salvinelli, A. Brinkman, M. Huijben, G. Koster, H. Hilgenkamp, G. Rijnders, D. Visentin, and L. Sangaletti, Band offsets and density of Ti³⁺ states probed by x-ray photoemission on LaAlO₃/SrTiO₃ heterointerfaces and their LaAlO₃ and SrTiO₃ bulk precursors, *Phys. Rev. B* **87**, 075435 (2013).
- [30] U. Treske, N. Heming, M. Knupfer, B. Büchner, E. D. Gennaro, A. Khare, U. S. Di Uccio, F. M. Granozio, S. Krause, and A. Koitzsch, Universal electronic structure of polar oxide heterointerfaces, *Sci. Rep.* **5**, 14506 (2015).
- [31] J. Gabel, M. Zapf, P. Scheiderer, P. Schütz, L. Dudy, M. Stübinger, C. Schlueter, T.-L. Lee, M. Sing, and R. Claessen, Disentangling specific versus generic doping mechanisms in oxide heterointerfaces, *Phys. Rev. B* **95**, 195109 (2017).
- [32] K. Yoshimatsu, R. Yasuhara, H. Kumigashira, and M. Oshima, Origin of Metallic States at the Heterointerface between the Band Insulators LaAlO₃ and SrTiO₃, *Phys. Rev. Lett.* **101**, 026802 (2008).
- [33] M. Sing, G. Berner, K. Goß, A. Müller, A. Ruff, A. Wetscherek, S. Thiel, J. Mannhart, S. A. Pauli, C. W. Schneider, P. R. Willmott, M. Gorgoi, F. Schäfers, and R. Claessen, Profiling the Interface Electron Gas of LaAlO₃/SrTiO₃ Heterostructures with Hard X-Ray Photoelectron Spectroscopy, *Phys. Rev. Lett.* **102**, 176805 (2009).
- [34] E. Slooten, Z. Zhong, H. J. A. Molegraaf, P. D. Eerkes, S. de Jong, F. Masee, E. van Heumen, M. K. Kruijze, S. Wenderich, J. E. Kleibeuker, M. Gorgoi, H. Hilgenkamp, A. Brinkman, M. Huijben, G. Rijnders, D. H. A. Blank, G. Koster, P. J. Kelly, and

- M. S. Golden, Hard x-ray photoemission and density functional theory study of the internal electric field in SrTiO₃/LaAlO₃ oxide heterostructures, *Phys. Rev. B* **87**, 085128 (2013).
- [35] M. Reinle-Schmitt, C. Cancellieri, D. Li, D. Fontaine, M. Medarde, E. Pomjakushina, C. Schneider, S. Gariglio, P. Ghosez, J.-M. Triscone, and P. Willmott, Tunable conductivity threshold at polar oxide interfaces, *Nat. Commun.* **3**, 932 (2012).
- [36] Y. Aiura, I. Hase, H. Bando, T. Yasue, T. Saitoh, and D. S. Dessau, Photoemission study of the metallic state of lightly electron-doped SrTiO₃, *Surf. Sci.* **515**, 61 (2002).
- [37] W. Meevasana, P. D. C. King, R. H. He, S.-K. Mo, M. Hashimoto, A. Tamai, P. Songsiririthigul, F. Baumberger, and Z.-X. Shen, Creation and control of a two-dimensional electron liquid at the bare SrTiO₃ surface, *Nat. Mater.* **10**, 114 (2011).
- [38] S. McKeown Walker, A. de la Torre, F. Y. Bruno, A. Tamai, T. K. Kim, M. Hoesch, M. Shi, M. S. Bahramy, P. D. C. King, and F. Baumberger, Control of a Two-Dimensional Electron Gas on SrTiO₃ (111) by Atomic Oxygen, *Phys. Rev. Lett.* **113**, 177601 (2014).
- [39] T. C. Rödel, C. Bareille, F. Fortuna, C. Baumier, F. Bertran, P. Le Fèvre, M. Gabay, O. Hijano Cubelos, M. J. Rozenberg, T. Maroutian, P. Lecoeur, and A. F. Santander-Syro, Orientational Tuning of the Fermi Sea of Confined Electrons at the SrTiO₃ (110) and (111) Surfaces, *Phys. Rev. Appl.* **1**, 051002(R) (2014).
- [40] L. Dudy, M. Sing, P. Scheiderer, J. D. Denlinger, P. Schütz, J. Gabel, M. Buchwald, C. Schlueter, T.-L. Lee, and R. Claessen, In situ control of separate electronic phases on SrTiO₃ surfaces by oxygen dosing, *Adv. Mater.* **28**, 7443 (2016).
- [41] G. Berner, M. Sing, H. Fujiwara, A. Yasui, Y. Saitoh, A. Yamasaki, Y. Nishitani, A. Sekiyama, N. Pavlenko, T. Kopp, C. Richter, J. Mannhart, S. Suga, and R. Claessen, Direct k-Space Mapping of the Electronic Structure in an Oxide-Oxide Interface, *Phys. Rev. Lett.* **110**, 247601 (2013).
- [42] G. Drera, F. Banfi, F. F. Canova, P. Borghetti, L. Sangaletti, F. Bondino, E. Magnano, J. Huijben, M. Huijben, G. Rijnders, D. H. A. Blank, H. Hilgenkamp, and A. Brinkman, Spectroscopic evidence of in-gap states at the SrTiO₃/LaAlO₃ ultrathin interfaces, *Appl. Phys. Lett.* **98**, 052907 (2011).
- [43] U. Treske, N. Heming, M. Knupfer, B. Büchner, A. Koitzsch, E. Di Gennaro, U. Scotti di Uccio, F. Mileto Granozio, and S. Krause, Observation of strontium segregation in LaAlO₃/SrTiO₃ and NdGaO₃/SrTiO₃ oxide heterostructures by X-ray photoemission spectroscopy, *APL Mater.* **2**, 012108 (2014).
- [44] See Supplemental Material at <http://link.aps.org/supplemental/10.1103/PhysRevB.108.045125> for details regarding possible Sr segregation, an analysis of O 1s spectra, photoelectron diffraction in the LaAlO₃ film, and complementary data and analysis for the (111) LaAlO₃/SrTiO₃ heterointerface, which includes Refs. [45,46].
- [45] S. Mukherjee, B. Pal, D. Choudhury, I. Sarkar, W. Drube, M. Gorgoi, O. Karis, H. Takagi, J. Matsuno, and D. D. Sarma, Origin and distribution of charge carriers in LaAlO₃-SrTiO₃ oxide heterostructures in the high carrier density limit, *Phys. Rev. B* **93**, 245124 (2016).
- [46] S. Hüfner, *Photoelectron Spectroscopy: Principles and Applications* (Springer, New York, 2003).
- [47] Y. Z. Chen, N. Bovet, T. Kasama, W. W. Gao, S. Yazdi, C. Ma, N. Pryds, and S. Linderoth, Room temperature formation of high-mobility two-dimensional electron gases at crystalline complex oxide interfaces, *Adv. Mater.* **26**, 1462 (2014).
- [48] P. Schütz, F. Pfaff, P. Scheiderer, Y. Z. Chen, N. Pryds, M. Gorgoi, M. Sing, and R. Claessen, Band bending and alignment at the spinel/perovskite γ -Al₂O₃/SrTiO₃ heterointerface, *Phys. Rev. B* **91**, 165118 (2015).
- [49] S. A. Chambers and P. V. Sushko, Probing energy landscapes in multilayer heterostructures: Challenges and opportunities, *APL Mater.* **7**, 110904 (2019).
- [50] S. A. Chambers, Y. Du, R. B. Comes, S. R. Spurgeon, and P. V. Sushko, The effects of core-level broadening in determining band alignment at the epitaxial SrTiO₃ (001)/p-Ge(001) heterojunction, *Appl. Phys. Lett.* **110**, 082104 (2017).
- [51] Y. Du, P. V. Sushko, S. R. Spurgeon, M. E. Bowden, J. M. Ablett, T.-L. Lee, N. F. Quackenbush, J. C. Woicik, and S. A. Chambers, Layer-resolved band bending at the n-SrTiO₃(001)/p-Ge(001) interface, *Phys. Rev. Mater.* **2**, 094602 (2018).
- [52] F. Stern, Self-consistent results for n-type Si inversion layers, *Phys. Rev. B* **5**, 4891 (1972).
- [53] F. Stern and W. E. Howard, Properties of semiconductor surface inversion layers in the electric quantum limit, *Phys. Rev.* **163**, 816 (1967).
- [54] G. L. Snider, I. Tan, and E. L. Hu, Electron states in mesaetched onedimensional quantum well wires, *J. Appl. Phys.* **68**, 2849 (1990).
- [55] I. Tan, G. L. Snider, L. D. Chang, and E. L. Hu, A selfconsistent solution of Schrödinger-Poisson equations using a nonuniform mesh, *J. Appl. Phys.* **68**, 4071 (1990).
- [56] J. Biscaras, N. Bergeal, S. Hurand, C. Grossetête, A. Rastogi, R. C. Budhani, D. LeBoeuf, C. Proust, and J. Lesueur, Two-Dimensional Superconducting Phase in LaTiO₃/SrTiO₃ Heterostructures Induced by High-Mobility Carrier Doping, *Phys. Rev. Lett.* **108**, 247004 (2012).
- [57] N. Scopigno, D. Bucheli, S. Caprara, J. Biscaras, N. Bergeal, J. Lesueur, and M. Grilli, Phase Separation from Electron Confinement at Oxide Interfaces, *Phys. Rev. Lett.* **116**, 026804 (2016).
- [58] A. E. M. Smink, J. C. de Boer, M. P. Stehno, A. Brinkman, W. G. van der Wiel, and H. Hilgenkamp, Gate-Tunable Band Structure of the LaAlO₃ - SrTiO₃ Interface, *Phys. Rev. Lett.* **118**, 106401 (2017).
- [59] D. Li, S. Lemal, S. Gariglio, Z. Wu, A. Fête, M. Boselli, P. Ghosez, and J.-M. Triscone, Probing quantum confinement and electronic structure at polar oxide interfaces, *Adv. Sci.* **5**, 1800242 (2018).
- [60] C. Yin, A. E. M. Smink, I. Leermakers, L. M. K. Tang, N. Lebedev, U. Zeitler, W. G. van der Wiel, H. Hilgenkamp, and J. Aarts, Electron Trapping Mechanism in LaAlO₃/SrTiO₃ Heterostructures, *Phys. Rev. Lett.* **124**, 017702 (2020).
- [61] Program available at <https://www3.nd.edu/~gsnider/>.
- [62] E. Y. Tsymlal, E. R. A. Dagotto, C.-B. Eom, and R. Ramesh (eds.), *Multifunctional Oxide Heterostructures* (Oxford University Press, Oxford, 2012).
- [63] C. Lin and A. A. Demkov, Electron Correlation in Oxygen Vacancy in SrTiO₃, *Phys. Rev. Lett.* **111**, 217601 (2013).
- [64] W. Demtröder, *Elektrostatik* (Springer, Berlin, Heidelberg, 2017).

- [65] A. Fête, Magnetotransport experiments at the LaAlO₃/SrTiO₃ interface, Ph.D. thesis, Université de Genève, 2014.
- [66] H.-M. Christen, J. Mannhart, E. J. Williams, and C. Gerber, Dielectric properties of sputtered SrTiO₃ films, *Phys. Rev. B* **49**, 12095 (1994).
- [67] S. Gariglio, M. Gabay, and J.-M. Triscone, Research Update: Conductivity and beyond at the LaAlO₃/SrTiO₃ interface, *APL Materials* **4**, 060701 (2016).
- [68] H. Peelaers, K. Krishnaswamy, L. Gordon, D. Steiauf, A. Sarwe, A. Janotti, and C. G. Van de Walle, Impact of electric-field dependent dielectric constants on two-dimensional electron gases in complex oxides, *Appl. Phys. Lett.* **107**, 183505 (2015).
- [69] $\lambda_{\text{IMFP,Ti } 2p} = 40.8 \text{ \AA}$ estimated by the TPP-2M formula [70–72].
- [70] S. Tanuma, C. J. Powell, and D. R. Penn, Calculations of electron inelastic mean free paths. V. Data for 14 organic compounds over the 502000 eV range, *Surf. Interface Anal.* **21**, 165 (1994).
- [71] S. Tanuma, C. J. Powell, and D. R. Penn, Calculation of electron inelastic mean free paths (IMFPs) VII. Reliability of the TPP-2M IMFP predictive equation, *Surf. Interface Anal.* **35**, 268 (2003).
- [72] C. J. Powell and A. Jablonski, NIST Electron Inelastic-Mean-Free-Path Database 71 - Version 1.1 (National Institute of Standards and Technology, Gaithersburg, 2000).
- [73] $\lambda_{\text{IMFP,Sr } 3d} = 45.0 \text{ \AA}$ estimated by the TPP-2M formula [70–72].
- [74] We assume that the polarisability of oxygen-deficient STO is comparable to stoichiometric SrTiO₃. Considering also the fact that the maximum V_O concentration in our heterostructures is on the order of only 10 at. %, we can safely ignore the dependence of ϵ_r of SrTiO₃ on the V_O concentration to simplify our model.
- [75] M. Marques, Jr., L. K. Teles, V. Anjos, L. M. R. Scolfaro, J. R. Leite, V. N. Freire, G. A. Farias, and E. F. da Silva, Full-relativistic calculations of the SrTiO₃ carrier effective masses and complex dielectric function, *Appl. Phys. Lett.* **82**, 3074 (2003).
- [76] T. Okuda, K. Nakanishi, S. Miyasaka, and Y. Tokura, Large thermoelectric response of metallic perovskites: Sr_{1-x}La_xTiO₃ (0 ≤ x ≤ 0.1), *Phys. Rev. B* **63**, 113104 (2001).
- [77] Z. Q. Liu, C. J. Li, W. M. Lü, X. H. Huang, Z. Huang, S. W. Zeng, X. P. Qiu, L. S. Huang, A. Annadi, J. S. Chen, J. M. D. Coey, T. Venkatesan, and Ariando, Origin of the Two-Dimensional Electron Gas at LaAlO₃/SrTiO₃ Interfaces: The Role of Oxygen Vacancies and Electronic Reconstruction, *Phys. Rev. X* **3**, 021010 (2013).
- [78] The SrTiO₃ and LaAlO₃ reference spectra are recorded at the same photon energy under oxygen dosing from a Nb doped SrTiO₃ substrate and a 20 uc thick LaAlO₃/SrTiO₃ heterostructure, respectively.
- [79] E. A. Kraut, R. W. Grant, J. R. Waldrop, and S. P. Kowalczyk, Precise Determination of the Valence-Band Edge in X-Ray Photoemission Spectra: Application to Measurement of Semiconductor Interface Potentials, *Phys. Rev. Lett.* **44**, 1620 (1980).
- [80] Z. Zhong and P. Hansmann, Band Alignment and Charge Transfer in Complex Oxide Interfaces, *Phys. Rev. X* **7**, 011023 (2017).
- [81] N. Nakagawa, H. Y. Hwang, and D. A. Muller, Why some interfaces cannot be sharp, *Nat. Mater.* **5**, 204 (2006).
- [82] C. Weiland, G. E. Sterbinsky, A. K. Rumaiz, C. S. Hellberg, J. C. Woicik, S. Zhu, and D. G. Schlom, Stoichiometry dependence of potential screening at La_(1-δ)Al_(1+δ)O₃/SrTiO₃ interfaces, *Phys. Rev. B* **91**, 165103 (2015).
- [83] R. Pentcheva and W. E. Pickett, Avoiding the Polarization Catastrophe in LaAlO₃ Overlayers on SrTiO₃(001) through Polar Distortion, *Phys. Rev. Lett.* **102**, 107602 (2009).
- [84] L. Yu and A. Zunger, A polarity-induced defect mechanism for conductivity and magnetism at polaron-polar oxide interfaces, *Nat. Commun.* **5**, 5118 (2014).
- [85] Z. Zhong, P. X. Xu, and P. J. Kelly, Polarity-induced oxygen vacancies at LaAlO₃/SrTiO₃ interfaces, *Phys. Rev. B* **82**, 165127 (2010).
- [86] N. C. Bristowe, P. B. Littlewood, and E. Artacho, Surface defects and conduction in polar oxide heterostructures, *Phys. Rev. B* **83**, 205405 (2011).
- [87] Y. Li, S. N. Phattalung, S. Limpijumnong, J. Kim, and J. Yu, Formation of oxygen vacancies and charge carriers induced in the n-type interface of a LaAlO₃ overlayer on SrTiO₃(001), *Phys. Rev. B* **84**, 245307 (2011).
- [88] N. Pavlenko, T. Kopp, E. Y. Tsybal, J. Mannhart, and G. A. Sawatzky, Oxygen vacancies at titanate interfaces: Two-dimensional magnetism and orbital reconstruction, *Phys. Rev. B* **86**, 064431 (2012).
- [89] Most of the photoemission studies have been conducted at room temperature while our data has been taken at 60 K. However, in further experiments we found that the electronic interface properties as, e.g., the 2DES extension do barely change between 60 K and 300 K due to the peculiar electric field dependence of the SrTiO₃ dielectric constant [93].
- [90] The samples are labeled according to the deposition conditions stated and by the Ti³⁺ weight: The samples are labeled as fully oxidized when the authors indicate that they post-oxidize the samples in a high oxygen background pressure >10 mbar after the LaAlO₃ deposition. However, when samples are deposited at an oxygen partial pressure of >10⁻² mbar, they might also be fully oxidized even without a further post-oxidation process. To estimate the V_O concentration in such samples, we resort to the Ti³⁺ weight whenever possible and classify the samples as fully oxidized if the Ti³⁺ weight lies below ≈ 3%.
- [91] Y. Xie, Y. Hikita, C. Bell, and H. Y. Hwang, Control of electronic conduction at an oxide heterointerface using surface polar adsorbates, *Nat. Commun.* **2**, 494 (2011).
- [92] P. Scheiderer, F. Pfaff, J. Gabel, M. Kamp, M. Sing, and R. Claessen, Surface-interface coupling in an oxide heterostructure: Impact of adsorbates on LaAlO₃/SrTiO₃, *Phys. Rev. B* **92**, 195422 (2015).
- [93] O. Copie, V. Garcia, C. Bödefeld, C. Carrétéro, M. Bibes, G. Herranz, E. Jacquet, J.-L. Maurice, B. Vinter, S. Fusil, K. Bouzouhane, H. Jaffrès, and A. Barthélémy, Towards Two-Dimensional Metallic Behavior at LaAlO₃/SrTiO₃ Interfaces, *Phys. Rev. Lett.* **102**, 216804 (2009).